iScience

CellPress
OPEN ACCESS

Review

Biomedical Applications of Tissue Clearing and Three-Dimensional Imaging in Health and Disease

Maria Victoria Gómez-Gaviro,[1,2,3,*] Daniel Sanderson,[1,3] Jorge Ripoll,[1,3] and Manuel Desco[1,2,3,4]

SUMMARY

Three-dimensional (3D) optical imaging techniques can expand our knowledge about physiological and pathological processes that cannot be fully understood with 2D approaches. Standard diagnostic tests frequently are not sufficient to unequivocally determine the presence of a pathological condition. Whole-organ optical imaging requires tissue transparency, which can be achieved by using tissue clearing procedures enabling deeper image acquisition and therefore making possible the analysis of large-scale biological tissue samples. Here, we review currently available clearing agents, methods, and their application in imaging of physiological or pathological conditions in different animal and human organs. We also compare different optical tissue clearing methods discussing their advantages and disadvantages and review the use of different 3D imaging techniques for the visualization and image acquisition of cleared tissues. The use of optical tissue clearing resources for large-scale biological tissues 3D imaging paves the way for future applications in translational and clinical research.

INTRODUCTION

In the last few decades, huge advances have been made in non-invasive imaging techniques, including the development of magnetic resonance imaging (MRI), positron emission transmission (PET), and computed tomography (CT) (Azaripour et al., 2016). These technologies produce 3D images, which enable good visualization of the anatomy and structure of human and animal tissues (Anzai et al., 2019). From a clinical point of view, the resolution provided by these techniques is sufficient, in the sense that cellular accuracy is not required for diagnosis or treatment. However, in some studies, it is necessary to acquire images at subcellular resolution while maintaining the 3D structure. A prime example of this need is the study of neuronal circuitry (Sato et al., 2019). A thorough analysis of the neuronal connections in the brain requires 3D images at cellular or even subcellular resolution. The aforementioned clinical imaging modalities enable non-invasive 3D imaging but do not reach cellular resolution, necessary to provide information about the tissue cytoarchitecture. Also, in most cases it lacks sufficient specificity as to identify different cell populations and therefore cannot be used for this purpose, at least for the time being.

At the other end of the spectrum, histological techniques provide high-resolution cellular and subcellular 2D images but require the tissue under study to be cut into thin slices. However, when the tissue is cut into sections, the 3D structure of the organ becomes difficult to reconstruct. Although some image processing programs are designed to generate histological 3D reconstructions such as FIJI (Schindelin et al., 2012), MATLAB (Křížek et al., 2016), Imaris (Haass-Koffler et al., 2012), and Amira (Hikspoors et al., 2017), image stacking is rather laborious, leads to anisotropic resolution, and may not be reliable if slices undergo deformation. Consequently, it is difficult to achieve high-resolution 3D reconstructions even after correcting stripes and illumination artifacts with preprocessing methods such as the "rolling ball" algorithm implemented in MATLAB (Leischner et al., 2010) and the "N4"-Algorithm implemented in 3DSlicer (Fedorov et al., 2012).

Alternative optical imaging modalities, such as confocal microscopy, generate highly accurate 3D images and are frequently used with fluorophore-stained samples (Willadsen et al., 2018). A confocal microscope is similar to a normal fluorescence microscope in the sense that it illuminates the sample with light of a specific wavelength, which is absorbed by fluorophores that re-emit light of longer wavelengths. Confocal

[1]Instituto de Investigación Sanitaria Gregorio Marañón, Madrid, Spain

[2]Centro de Investigación Biomédica en Red de Salud Mental (CIBERSAM), Madrid, Spain

[3]Departamento de Bioingeniería e Ingeniería Aeroespacial, Universidad Carlos III de Madrid, Madrid, Spain

[4]Centro Nacional de Investigaciones Cardiovasculares Carlos III, Madrid, Spain

*Correspondence: vgomez@hggm.es

https://doi.org/10.1016/j.isci.2020.101432

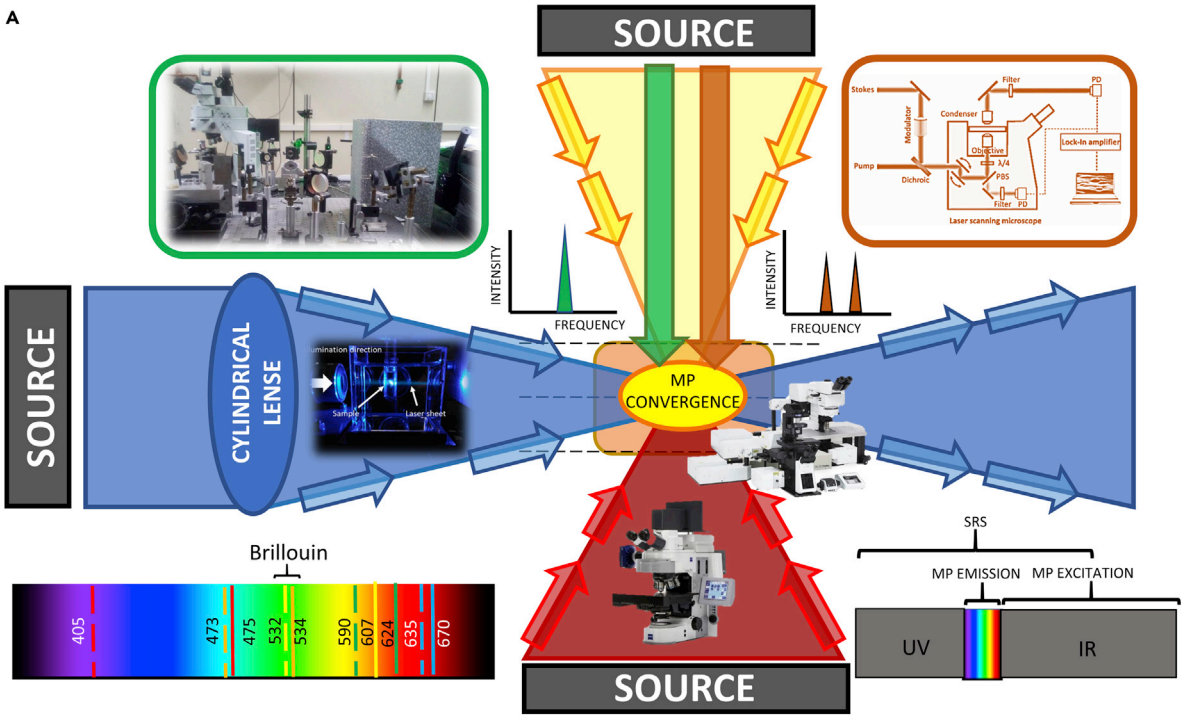
A
SOURCE
Stokes
Filter
PD
Condenser
Modulator
Objective
Lock-In amplifier
Pump
λ/4
Dichroic
PBS
Filter
PD
Laser scanning microscope
INTENSITY
FREQUENCY
INTENSITY
FREQUENCY
SOURCE
CYLINDRICAL LENSE
MP CONVERGENCE
Brillouin
405
473
475
532
534
590
607
624
635
670
SRS
MP EMISSION
MP EXCITATION
UV
IR
SOURCE

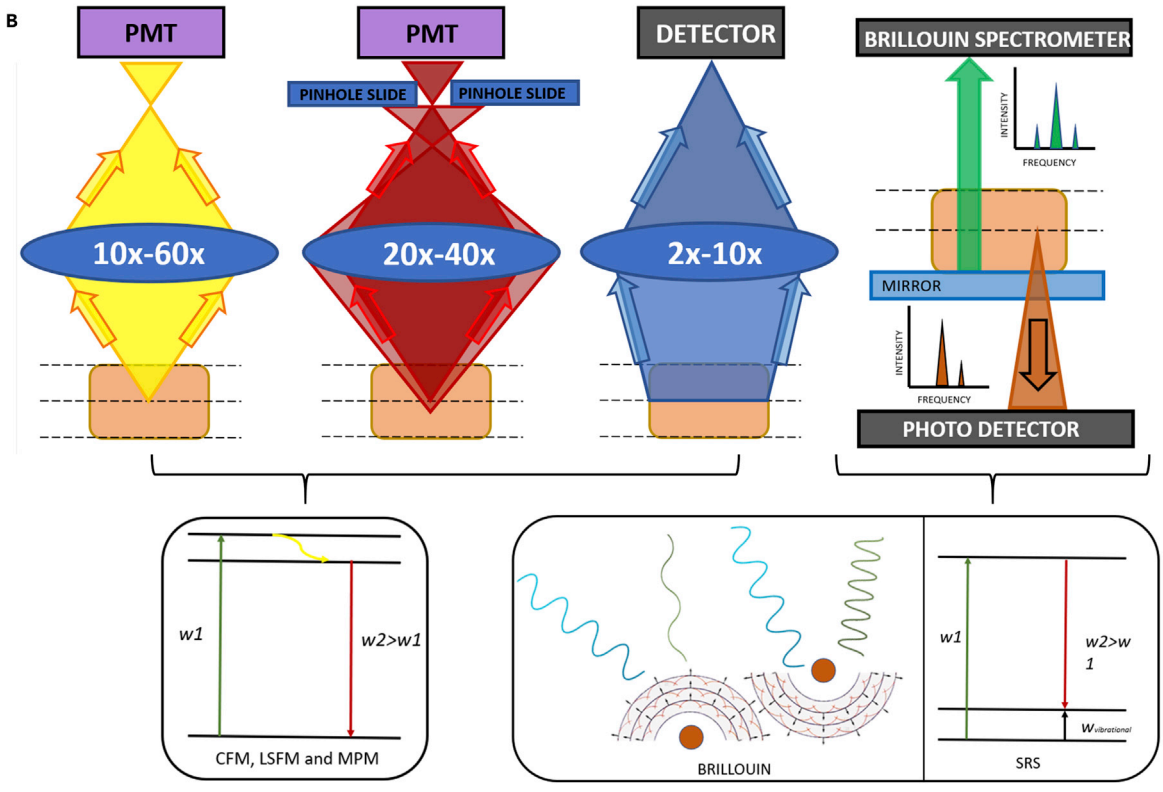
B
PMT
PMT
DETECTOR
BRILLOUIN SPECTROMETER
PINHOLE SLIDE
PINHOLE SLIDE
10x-60x
20x-40x
2x-10x
INTENSITY
FREQUENCY
MIRROR
INTENSITY
FREQUENCY
PHOTO DETECTOR
w1
w2>w1
CFM, LSFM and MPM
BRILLOUIN
w1
w2>w1
SRS

Figure 1. Schematic Showing the Fundamental Physics and Functioning of the Imaging and Spectroscopic Techniques Considered in This Review

The biological sample is represented by a central brown rectangle, the objective by a blue ellipsoid, the photodetectors by purple boxes, and the laser emitters and detector by a black box. Blue: LSFM. Red: confocal microscopy. Green: Brillouin spectroscopy. Yellow: Multiphoton microscopy. Brown: SRS microscopy. Brillouin and Raman graphs represent laser intensity versus frequency. Confocal and Raman microscopes may irradiate the sample from the opposite direction too.

(A) Input from the different 3D imaging systems. Each color represents the laser beam produced by the source of each imaging system. Discontinuous lines in the color spectrum represent commonly used excitation wavelengths (nm) in LSFM, and continuous lines represent in the same color the peak wavelength of the corresponding emission filters used. Raman microscope image was adapted from Stimulated Raman Scattering Microscopy (https://www.castl.uci.edu/sites/default/files/Min%20SS%20presentation.pdf), Confocal microscope image was adapted from Zeiss microscopy (https://www.zeiss.com/microscopy/int/products/confocal-microscopes/lsm-900-for-materials-non-contact-surface-topography-in-3d.html).

(B) Output of the 3D imaging systems. Each color represents the laser beam obtained from the sample. Below each imaging system, the physical mechanism on which each one is based is graphically shown. Confocal, multiphoton, and LSFM microscopies are based on fluorescence, whereas Brillouin is based on phonon detection and Raman microscopy on stimulated Raman scattering. Magnification objective range from MP was retrieved from Singh et al. (2015).

microscopes can create thin 3D images by detecting fluorescence light produced at the focal spot and by moving the position of this spot. That is, instead of exciting the entire specimen evenly and detecting fluorescence emitted from the whole sample, confocal microscopy excludes out-of-focus fluorescence (Figures 1).

Nevertheless, optical imaging is hampered by reduced light penetration when a tissue or organ is not transparent. The main causes leading to tissue opacity are refractive index (RI) mismatch between lipid and aqueous media interfaces (Chung et al., 2013) and non-homogeneous distribution of scatterers (Richardson and Lichtman, 2015), mainly lipids, collagen fibers, and myofibrils. Light absorption is a minor cause of tissue opacity in mammals, as very few chromophores can absorb electromagnetic waves in the visible range; hence, light absorption can be almost disregarded in tissues that are not rich in heme groups or melanin (Inyushin et al., 2019). It is important to notice that this is not the case of invertebrates or several animal species, in which pigments such as ommochromes or pterins constitute a significant cause of opacity, and for which particular depigmentation clearing protocols have been specifically developed, such as DEpigmEntation-Plus-Clearing (DEEP-Clear) (Pende et al., 2020) or FlyClear (Pende et al., 2018), which can also eliminate heme groups and melanin. But in most studied mammals whatsoever, lipids and RI mismatch are the major factors that lead light to be scattered instead of traveling straight through the tissue, causing blurring and opacity. Non-transparent tissues are therefore not suitable for the acquisition of high-resolution images (Kolesová et al., 2016). Thus, obtaining high-accuracy 3D images makes it necessary to turn tissues or organs transparent using clearing agents. In some cases (e.g., benzyl alcohol/benzyl benzoate [BABB]), the sample must be fixed and dehydrated (Dodt et al., 2007; Genina et al., 2010) before being immersed in a clearing agent. Some clearing agents like CUBIC (clear, unobstructed brain image cocktails and computational analysis) (Susaki et al., 2014) reduce lipid content. CUBIC also induces tissue swelling, reducing the overall RI as predicted by the Lorentz-Lorenz equation and, therefore, facilitating RI matching (Ueda et al., 2020). For a summary of the different steps that can be followed by most optical clearing methods see Figure 2.

In general, clearing agents improve light penetration by eliminating lipids and natural pigments matching the tissue refractive indices (RIs). Spatial distribution of different structures in tissue can serve to evaluate the functional status of an organ, for example, in the case of the muscle (Yin et al., 2019).

Human tissues like placenta, myocardial tissue, and some others have been optically cleared successfully, enabling a deeper comprehension of the 3D microanatomy and cytoarchitecture of the tissues and bringing light for more accurate diagnosis and treatments. In the case of the placenta, it allowed a better evaluation of the morphology and transport capacities of placental blood barriers (Carrillo et al., 2018), whereas in the case of myocardial tissue it has been used to evaluate the organization of collagen in healthy hearts and in heart failure tissue (Perbellini et al., 2017). Optical clearing has also been presented as a powerful 3D histopathology tool for pancreatic lesions diagnosis (Hong et al., 2019), in order to detect and visualize endocrine and exocrine pathologies and to evaluate the 3D architecture of neoplasia lesions and adenocarcinomas (Matryba et al., 2019). In fact, cellular resolution is fundamental for early diagnosis, as several diseases arise as a direct consequence of changes in cellular structure and behavior (Antonacci and Braakman, 2016) even before they are fully noticed. Technological advances in the microscopy field have allowed 3D imaging techniques to achieve such resolution.

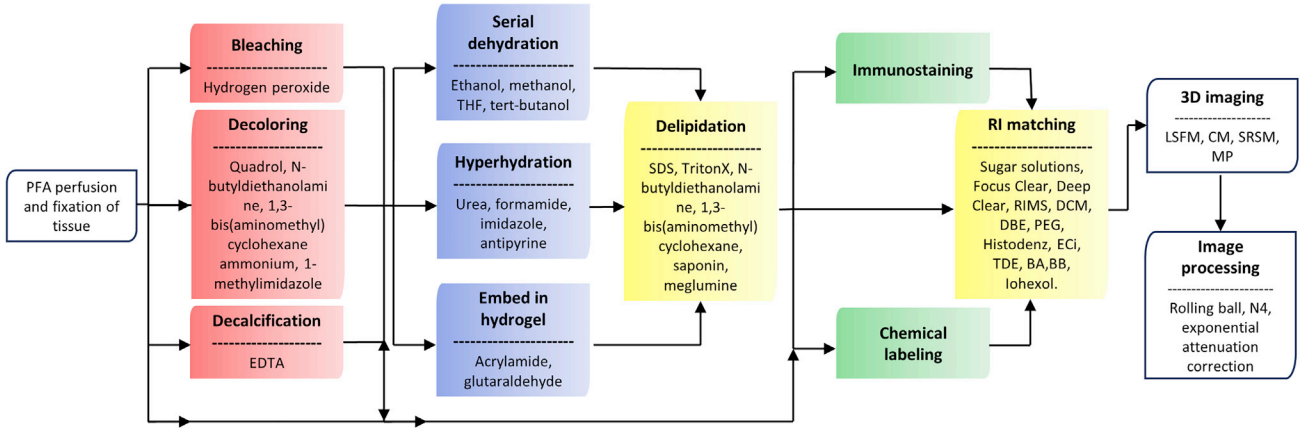

Figure 2. Workflow Summarizing the Different Possible Steps that an Optical Clearing Method Can Follow to Render a Whole Organ Transparent
The chosen pipeline will depend on the properties of the tissue that is going to be treated and on the specific goals desired. Each box represents a specific physical or chemical procedure and the most common substances used to achieve it.

TRANSPARENCY AND TISSUE CLEARING METHODS

Tissue opacity, which results from light absorption and scattering, prevents light from penetrating the sample and thus impairs excitation of fluorescent proteins, such as green fluorescence protein (GFP) or labeled antibodies.

Comprehensive analyses of histological sections are limited by poor penetration of the antibodies and laser light. Clearing protocols increase transparency and improve not only penetration of laser light but also diffusion of antibodies into the sample (Nehrhoff et al., 2016), thus enabling the analysis of thick layers of biological tissue.

Most available clearing agents are inspired organic solvents (Costantini et al., 2019), such as BABB or benzyl alcohol/glycerol (Pires et al., 2016), which generally have fast clearing dynamics (Qi et al., 2019). However, alcohols present in these organic solvents have been reported to quench and weaken the fluorescence signal in organs (Dodt et al., 2007; Genina et al., 2010). New organic solvent-based methods such as uDISCO (Pan et al., 2016), FDISCO (Qi et al., 2019), or sDISCO (Hahn et al., 2019), which are described in further detail below, have been developed to overcome this issue and better preserve fluorescence. Table 1 summarizes the main characteristics of several clearing agents and how they affect the physical properties of the tissue (Kim et al., 2018).

In contrast, other clearing agents such as Clear^{T} and Clear^{T2} do not contain organic solvents (Cai et al., 2019). It has been reported that Clear^{T2} does not disrupt the fluorescence signal and that Clear^{T} clears organs faster than BABB (Kuwajima et al., 2013). However, Clear^{T} is incompatible with immunohistochemistry and genetically encoded fluorescent proteins, such as GFP, and the clearing power of Clear^{T2} is not strong enough. As an alternative, a new clearing method has been recently developed, called RTF, which is based on Clear^{T2}. It shows better clearing capacity while preserving compatibility with immunostaining and endogenous fluorescence signals (Yu et al., 2018). CLARITY (clear lipid-exchanged acrylamide-hybridized rigid imaging/immunostaining/*in situ* hybridization-compatible tissue-hydrogel) was also developed to overcome fluorescence quenching of organic solvent-based clearing protocols and to better preserve tissue structure at a subcellular level when performing *in situ* hybridization of the sample (Chung et al., 2013). Combining CLARITY with ETC (electrophoretic tissue clearing) renders faster results by using charged micelles for electrophoretic extraction of lipids (Chung et al., 2013). CLARITY uses SDS for this step owing to its amphipaticity (Table 2), which makes it ideal for this kind of micelle-mediated lipid removal. However, excessive heating can damage the sample, so PACT (Passive Clarity Technique) was developed to perform passive clearing at a faster speed by facilitating the diffusion of SDS. This is achieved by reducing the density of the hydrogel and by excluding CLARITY's bis-acrylamide cross-linker (Yang et al., 2014b). As an RI matching solution, PACT can make use of RC-CD (PACT-RC) (Lloyd-Lewis et al., 2016), RIMS (Yang et al., 2014b), or sRIMS (PACT-sRIMS), which uses Sorbitol to provide RIMS with clearing capacity (Treweek

Clearing Agent	Chemical Composition	Solvent	Tissue Tested	Size Change (Expansion/ Shrinkage)	Protocol Length	IHC Compatibility	Native Fluorescence Quenching	Reference
ACT-PRESTO	Hydrogel + SDS	S	Brain,	Shrinkage	Short	Y	N	(Lee et al., 2016)
Adipo-clear	Methanol, DCM, DBE, Triton X-	O	Adipose tissue	No	Short	Y	Y	(Chi et al., 2018)
a-UDISCO	Tert-butanol, BABB-D4 (benzyl alcohol, benzyl benzoate, vitamin E, diphenyl ether), dichloromethane, and triethylamine (pH adjustment to 9.0–9.5).	O	Mouse brain, muscle, stomach, and lung. Not recommended for heme-rich tissues such as heart, spleen, liver, and kidney	Shrinkage (like uDISCO: 65% in volume)	Short (19 h)	N.D.	N (less than uDISCO)	(Li et al., 2018)
BABB	33% Benzyl alcohol, 67% benzyl benzoate	O	Mouse embryo, brain, tumor, kidney, human aorta, lung	Shrinkage	Short	Y (before clearing)	Y	(Dodt et al., 2007) (Genina et al., 2010)
BAG	55% Benzyl alcohol 45% Glycerol	O	?	Shrinkage	Short	Y (before clearing)	Y	(Dodt et al., 2007) (Genina et al., 2010)
BoneCLARITY	10% EDTA, 4% acrylamide, SDS, RIMS	S	Mouse femur, tibia, and vertebral column	Swelling	Very long (28 d)	Y	N	(Greenbaum et al., 2017)
Ce3D	N-methyl acetamide, Histodenz, 1-thioglycerol, Triton X-	Y	Bone, lung, kidney, intestine, lymph nodes, liver, muscle, thymus, brain	Very slight shrinkage	Short	Y	N	(Li et al., 2017)
CLARITY	SDS, acrylamide	S	Whole body, mouse embryo, mouse heart, brain, lung,	Shrinkage	Very long	Y	N	(Chung et al., 2013)
Clear^{T}	100% Formamide	A	Mouse brain and embryos	N	Medium	N	Y	(Kuwajima et al., 2013)
Clear^{T2}	Formamide and PEG	A	Liver	N	Medium	Y	N	(Kuwajima et al., 2013)
CRISTAL	Ethanol, xylene, resin	O	Rat lung, brain, bone	Not mentioned	5 d - 3 w	Y	Y	(Kellner et al., 2016)

Table 1. Main Features of Clearing Reagents and Methods

(Continued on next page)

Clearing Agent	Chemical Composition	Solvent	Tissue Tested	Size Change (Expansion/ Shrinkage)	Protocol Length	IHC Compatibility	Native Fluorescence Quenching	Reference
CUBIC Advanced CUBIC	Polyalcohols, triton, urea, sucrose, nitriloethanol	A	Whole body, mouse and chicken embryo, mouse brain, lung, human intestine, adult mouse heart, mammary gland, liver, lung carcinoma	Expansion	Medium	Y	Y	(Susaki and Ueda, 2016; Susaki et al., 2014)
CUBIC1	CUBIC-L (10 wt % N-butyldiethanolamine, 10 wt % Triton X-100), CUBIC-P (5 wt % 1-methylimidazole, 10 wt % N-butyldiethanolamine), 10 wt % Triton X-100 CUBIC-R (5 wt % antipyrine, 30 wt % nicotinamide, optionally pH 8–9 adjusted by N-butyldiethanolamine), or CUBIC-RA 5 wt % antipyrine, 30 wt % N-methylnicotinamide, optionally pH 8–9 adjusted by N-butyldiethanolamine	A	Mouse brain and kidney	N (for neutral pH of CUBIC-R)	Medium (5–9 d)	Y	N	(Tainaka et al., 2018)
CUBIC2	CUBIC-L, CUBIC-P, CUBIC-B (10 wt % EDTA, 15 wt % imidazole) and CUBIC-R or CUBIC-RA	A	Mouse leg, head, spine, and whole body	N (for neutral pH of CUBIC-R)	Long (12–21 d)	Y	N	(Tainaka et al., 2018)
CUBIC3	CUBIC-HL (10 wt % 1,3-bis(aminomethyl)cyclohexane, 10 wt % sodium dodecylbenzene sulfonate, pH 12.0 adjusted by p-toluene sulfonic acid), CUBIC-R	A	Human heart and kidney	N (for neutral pH of CUBIC-R)	Medium (9–16 d)	Y	Y	(Tainaka et al., 2018)
CUBIC4	CUBIC-L, CUBIC-R	A	Human brain	N (for neutral pH of CUBIC-R)	Medium (9–16 d)	Y	N	(Tainaka et al., 2018)
CUBIC-cancer	CUBIC-L, modified CUBIC-R (45 wt % antipyrine and 30 wt % nicotinamide)	A	Mouse liver, intestine, pancreas, lung, brain	Minimal	Medium (10 d)	Y	N	(Kubota et al., 2017; Richardson and Lichtman, 2017)
CUBIC-HistoVIsion	CUBIC clearing, 500 mM NaCl, HEPES buffer, 0.5% casein, Quadrol, urea, collagenase P	A	Marmoset whole body, mouse brain, human cerebellum	Swelling	Very long (11 d - 2.5 m)	Y	N	(Susaki et al., 2020)

Table 1. *Continued*

(Continued on next page)

Clearing Agent	Chemical Composition	Solvent	Tissue Tested	Size Change (Expansion/ Shrinkage)	Protocol Length	IHC Compatibility	Native Fluorescence Quenching	Reference
CUBIC-X	CUBIC-R1 (Polyalcohols, triton, urea), CUBIC-X1 (20% imidazole), CUBIC-X2 (5% imidazole, 55% antipyrine cocktail)	A	Mouse brain	Swelling	Long (2–3 w)	Y	N	(Murakami et al., 2018)
DBE	Dibenzyl ether	A	Mouse brain	N	Short	Y (before clearing)	N	(Becker et al., 2012)
DEEP-clear	FlyClear solution 1 1 (N,N,N′,N′-Tetrakis(2-hydroxyethyl) ethylenediamine (THEED), Triton X-100, urea), acetone, hydrogen peroxide and solution 2 (meglumine diatrizoate)	A/O	Bristle worm, squid, Zebrafish, axolotl	N	Short (less than 1 d)	Y	N	(Pende et al., 2020)
3DISCO iDISCO	Tetrahydrofuran (THF) Dichloromethane Dibenzyl ether	O	Most mouse organs	Shrinkage	Short	Y	N Y (1–2 d lifetime)	(Becker et al., 2012) (Erturk et al., 2014)
ePACT	Hydrogel + 10% SDS-PBS (pH 8)	S	Mouse brain	Swelling	Medium (1–2 w)	Y	N	(Treweek et al., 2015)
Ethanol-ECi	Ethyl-3-phenylprop-2-enoate	O	Kidney, heart	Shrinkage	Short (4 d)	Y	N	(Klingberg et al., 2017)
EyeCi	ECi clearing + iDISCO immunolabeling	O	Mouse eye	Shrinkage	Short (1 w)	Y	?	(Decroix et al., 2015)' (Klingberg et al., 2017)
2ECi	1-propanol, ethyl cinnamate	O	Human cerebral organoids, whole axolotl, Xenopus, and Drosophila	Shrinkage	Short (25 h–5 d)	Y	N	(Masselink et al., 2019)
FACT	8% SDS, Focus Clear	O	Mouse brain	Shrinkage (slightly)	Medium (6 d-14 d)	Y	N	(Xu et al., 2017)
FASTClear	THF, DBE	O	Human myocardium	Shrinkage	Very fast (45 min)	Y	N.D.	(Perbellini et al., 2017)
FDISCO	4°C/pH 9.0 THF and 4°C DBE	O	Brain, kidney, muscle	Shrinkage (similar to 3DISCO)	short (3–4 d)	Y	N	(Qi et al., 2019)
FluoClearBABB	1-Propanol, tert-butanol	O	Mouse brain	Shrinkage	Medium (10 d)	?	N	(Schwarz et al., 2015)

Table 1. *Continued*

(Continued on next page)

Clearing Agent	Chemical Composition	Solvent	Tissue Tested	Size Change (Expansion/ Shrinkage)	Protocol Length	IHC Compatibility	Native Fluorescence Quenching	Reference
Fly-clear	Protease, acetone, Solution-1 (THEED, Triton X- and Urea), Solution-2 (meglumine diazotrate)	A/O	*Drosophila melanogaster*	N	Medium (1 w)	N.D.	Y	(Pende et al., 2018)
FRUIT	Fructose and urea	A	Rabbit brain	No shrinkage for 30% FRUIT	Short (4 d)	Y	Y	(Hou et al., 2015)
iDISCO+	Methanol, dichloromethane, dibenzyl ether	O	Mouse and rat brains	N	Very long (18 d)	Y	N.D.	(Renier et al., 2014) (Perin et al., 2019)
IsoScaleSQ	9.1 M urea, 22.5% (v/w) d-sorbitol, 200 mM sodium chloride, and 2% (v/w) Triton X-100.	A	Mouse brain	N	Very short (30 min)	Y (thin slices)	N	(Sato et al., 2019)
LUCID	TDE, glycerol, TBS, Tween 20	A	Porcine gastrointestinal mucosa	N	Short (5–7 d)	Y	N.D.	(Hildebrand et al., 2018)
MACS	MXDA, sorbitol	A	Murine brain, heart, lung, spleen, femur, and whole body	Slight expansion	Fast (2.5d)	Y	N	(Zhu et al., 2020)
MASH	DISCO with RIMS substituted by trans-cinnamaldehyde, TDE, and wintergreen oil	O	Human cortex	ND	Medium	Y	?	(Hildebrand et al., 2018)
MYOCLEAR	Hydrogel (VA-044, A4P0), PTwH	A	Mice diaphragm muscle	ND	Long (17 d)	Y	N	(Williams et al., 2019)
OPTIClear	20% w/v N-methylglucamine, 25% w/v 2,2′-thiodiethanol, 32% w/v Iohexol	A	Brain	N	Short (6 h)	Y (most abs)	Y (fluorescein, Alexa Fluor 488, Dylight dyes and rhodamine)	(Lai et al., 2018)
PACT	Hydrogel + SDS Optionally, sRIMS can be added	S	Lung mouse embryo	Shrinkage	Medium	Y	N	(Yang et al., 2014a)
PACT-deCAL	0.1 M EDTA in 1X PBS, 10% SDS-PBS, hydrogel	S	Tibia bone, vertebral column	?	Medium (1–2 w)	Y	?	(Treweek et al., 2015)
PARS	Hydrogel + SDS	S	Whole mouse, human tumor tissue	Shrinkage	Medium	Y	N	(Lai et al., 2018)

Table 1. *Continued*

(Continued on next page)

Clearing Agent	Chemical Composition	Solvent	Tissue Tested	Size Change (Expansion/ Shrinkage)	Protocol Length	IHC Compatibility	Native Fluorescence Quenching	Reference
Passive CLARITY	Nanoparticles	S	Mouse brain and spinal cord	Shrinkage	Very long	Y	N	(Roberts et al., 2016)
PEGASOS	Polyethylene glycol, 20% EDTA, 25% N, N,N′, N′-Tetrakis (2-hydroxypropyl) ethylenediamine, ammonium, PEGMMA, BB	O	Whole adult mouse body including bones but excluding pigmented epithelium	Shrinkage of soft tissues	Medium (7–12 d)	Y	N	(Jing et al., 2018)
ReagentF	2,2′,2″NItriloetahnol/Triethanolamide formamide	A	Neonatal mouse brain	?	Fast (1 d)	?	N	(Jianru et al., 2015)
RTF	Triethanolamine, formamide	A	Embryonic brain, embryo.	N	Short (h-1 d)	Y	Y	(Yu et al., 2018)
Scale	Urea, Triton X-, and glycerol	A	Mouse embryo, heart	N	Very long	N.D.	N	(Hama et al., 2011)
ScaleA2	Urea, glycerol, Triton X-	A	Mouse brain	Expansion	Long (w)	Incompatible with tropomyosin IHC	N	(Decroix et al., 2015) (Richardson and Lichtman, 2015)
ScaleS	Sorbitol-based Scale	A	Mouse brain	Slight expansion	Medium (6 d)	Y	N	(Hama et al., 2015) (Wan et al., 2018)
ScaleSQ	9.1 M Urea, 22.5% (w/w) sorbitol	A	Mouse brain	Strong expansion	Short (h)	Y	Y (slightly)	(Wan et al., 2018) (Costa et al., 2019)
SCM	CLARITY with a larger concentration of VA-044	O	Mouse heart	Expansion	Long (2–3 w)	Y	N	(Matryba et al., 2019; Richardson and Lichtman, 2017)
sDISCO	Hydroxytoluene, THF, BABB, DBE, propyl gallate	O	Mouse brain	Shrinkage (30% approx.)	Medium (1 w)	N.D.	N	(Hahn et al., 2019)
SeeDB	80.2% with a 0.5% α-thioglycerol in water	A	Brain, mammary gland	N	Medium	Y (brain)	Y	(Murakami et al., 2018), (Ke et al., 2016)
SeeDB2	Iohexol, saponin, and Tris-EDTA	A	Mouse brain	N	Short (2 d)	Y	N	(Ke et al., 2016)
SOCAs	Fructose, sucrose, PEG-400, propylene glycol, thiazine	O	Human skin	N	Short	Y	N	(Guo et al., 2016)
SUT	Urea, SDS, Triton X-, acrylamide, and PBS	A	Mouse, rat, and pigs' heart	ND	Depends on the species (4–29 d)	Y	N.D.	(Wang et al., 2018)

Table 1. *Continued*

(Continued on next page)

Clearing Agent	Chemical Composition	Solvent	Tissue Tested	Size Change (Expansion/ Shrinkage)	Protocol Length	IHC Compatibility	Native Fluorescence Quenching	Reference
SWITCH	Glutaraldehyde, sodium sulfite, 1-thioglycerol, SWITCH-off (PBS+0.5 mM SDS), SWITCH-on (PBST)	A	Human and rat brains Murine lung, heart, kidney, liver, and spinal cord	Warping	Medium (1–2 w)	Y	N.D.	(Murray et al., 2015)
TDE	97% 2,2′- Thiodiethanol in water	A	Brain	Shrinkage	Short	Combined with CLARITY	N	(Costantini et al., 2015)
UbasM	Ub-1 (1,3-Dimethyl-2-imidazolidinone, Meglumine, Triton X-, urea) and Ub-2 (urea, sucrose, and 1,3-dimethyl-2-imidazolidinone)	A	Mouse intestine, spleen, pancreas, heart, kidney, lung, liver, and brain	N	Medium (7–12 d)	Y	N	(Chen et al., 2017)
uDISCO	Diphenyl ether, benzyl alcohol, benzyl benzoate, vitamin E, tert-butanol	O	Brain, liver, lung, bone, whole rat	Shrinkage	4 d	Y	N	(Pan et al., 2016)
vDISCO	Tert-butanol 30%–100%, dichloromethane	O	Mouse brain, head, and meninges	Shrinkage	uDisco step: 4 d. Nano-boosting step: 10–12 d	Y	N (N.D. fluorescence conservation)	(Cai et al., 2019)

Table 1. *Continued*

PEG, polyethylene glycol; SDS, sodium dodecyl sulfate; O, organic solvent-based; A, aqueous-based; S, SDS; Y, yes; N, no; LN, lymphatic node; SOCAS, skin optical clearing agents; IHC, immunohistochemistry; h, hours; d, days; w, weeks; m, months; N.D., not defined.

Clearing Agent	MW (g/mol)	Chemical Formula	3D Conformer
SDS	288.3	$C_{12}H_{25}NaO_4S$	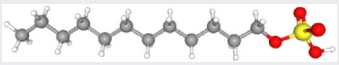
DCM	84.(Wei et al., 2019)	CH_2Cl_2	
DBE	198.2	$C_{14}H_{14}O$	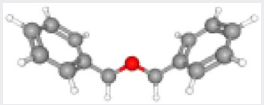
Triton X-	250.3	$C_{16}H_{26}O_2$	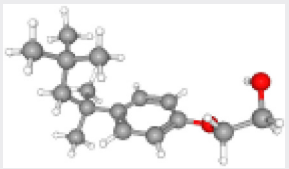
Benzyl alcohol	108.14	$C_6H_5CH_2OH$	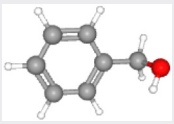
Benzyl benzoate	212.2	$C_{14}H_{12}O_2$	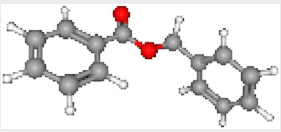
Triethanolamine	149.19	$C_6H_{15}NO_3$	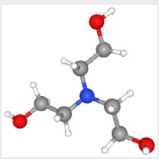
N,N,N′,N′-Tetrakis(2-hydroxypropyl) ethylenediamine (or Quadrol)	292.41	$C_{14}H_{32}N_2O_4$	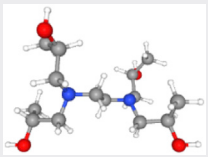
Sucrose	342.3	$C_{12}H_{22}O_{11}$	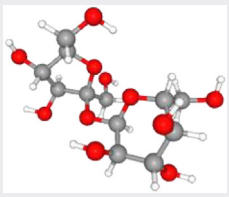

Table 2. Chemical Structure and Composition of Some of the Main Clearing Agents Currently Used

(Continued on next page)

Clearing Agent	MW (g/mol)	Chemical Formula	3D Conformer
Urea	60.056	NH_2CONH_2	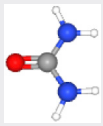
EDTA	292.24	$C_{10}H_{16}N_2O_8$	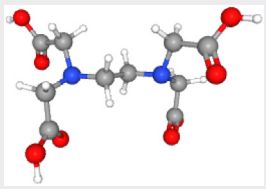
Glycerol	92.09	$C_3H_8O_3$	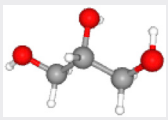
TDE	122.19	$C_4H_{10}O_2S$	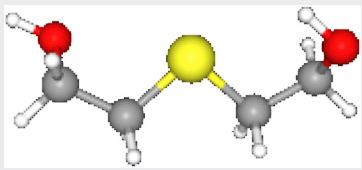
Acrylamide	71.08	C_3H_5NO	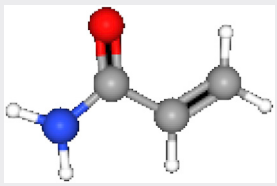
Antipyrine	188.2	$C_{11}H_{12}N_2O$	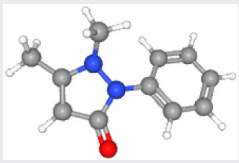
THF	72.11	C_4H_8O	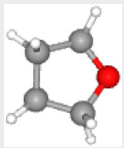
Ethyl cinnamate	176.2	$C_{11}H_{12}O_2$	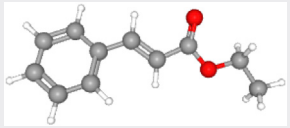

Table 2. *Continued*

(Continued on next page)

Clearing Agent	MW (g/mol)	Chemical Formula	3D Conformer
Fructose	180.16	$C_6H_{12}O_6$	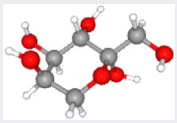
PEG	62.07	$(C_2H_4O)nH_2O$	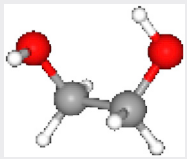
Saponin	1,223.3	$C_{58}H_{94}O_{27}$	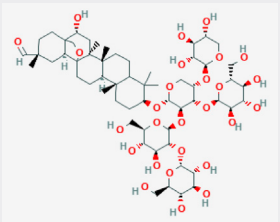
Tert-butanol	(Ke and Imai, 2014 #437).12	$C_4H_{10}O$	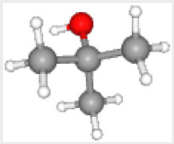
Sorbitol	182.17	$C_6H_{14}O_6$	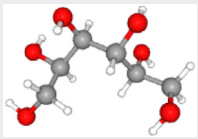
Methanol	32.04	CH4O	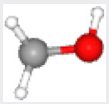

Table 2. *Continued*
Color code: gray: carbon atoms, white: hydrogen, red: oxygen, blue: nitrogen, green: chlorine, and yellow: sulfur. Images from PubChem.

et al., 2015). PACT's reagents can be perfused directly into the vasculature of the organ in larger samples (D. et al., Yang et al., 2014a).

As may be understood from Table 1, there is no "ideal" clearing agent. Each one presents pros and cons, and the researcher's choice may depend on the particular type of biological sample or experiment. To decide which clearing agent is the most appropriate for a specific analysis, we must take into consideration aspects such as organ or tissue under study, type of fluorescence, the importance of tissue shrinkage, and duration of the clearing. These aspects are individually addressed in the following paragraphs.

The specific organ or tissue under study is a relevant aspect since not all organs are cleared in the same way by the various agents. Clearing agents act differently on different tissues owing to their intrinsic structure and composition. For instance, it has been reported that CUBIC and PACT are the most appropriate clearing agents for the lungs of mouse embryos (Hirashima and Adachi, 2015; Yang et al., 2014a). CUBIC is a powerful and efficient clearing protocol that may be used in a great range of tissue types thanks to

the efficacy of the so-called CUBIC-1 and CUBIC-2 reagents, which can achieve delipidation and RI matching in a cheap and rapid way (Susaki et al., 2014). Conversely, FocusClear (a proprietary reagent), which is an RI matching solution, has been reported to be a quick clearing agent for visualization of the microvasculature in thick tissue sections of mouse brains (Moy et al., 2013). The intensity of the fluorescence signal is also relevant. For instance, organic solvents such as BABB (which quenches native fluorescence from endogenous proteins) may be used if the organ under study has strong transgenic fluorescence emission because the signal can still be detected or if antigen conjugated fluorophores are used (Sharpe et al., 2002). In contrast, for tissues with a weak fluorescence signal, it would be more appropriate to choose a clearing agent that better preserves fluorescence, such as Scale (Hama et al., 2011).

During tissue clearing, the organ is dehydrated and loses lipids and other components, thus reducing organ size and potentially altering its structure. For experiments in which structure and cell morphology are critical, it would be adequate to use 2,2′-thiodiethanol (TDE), which is an RI matching solution that hardly affects tissue structure (Costantini et al., 2015), or See Deep Brain (SeeDB) (Lloyd-Lewis et al., 2016), which does not reduce sample volume and maintains cell morphology intact in mouse brains. This is an important issue when studying neuronal circuits, in which the position and connections of neurons are analyzed in the context of the whole organ. Robustness of the tissue must also be considered when choosing a specific clearing protocol. For instance, large and mature organs are better cleared by SeeDB37ht rather than SeeDB, and fragile tissues such as embryonic brains, by using SeeDBp. Both are SeeDB variants that differ in the protocol length and duration of exposure to different fructose concentrations (Ke and Imai, 2014) (Ke et al., 2013). The time required for the clearing agent to turn the tissue transparent (clearing time) varies considerably depending on the organ and agent used. For instance, Clear^{T} turns embryonic mouse brains transparent much faster than Sca*l*e, which needs 2 weeks to achieve the transparency that Clear^{T} achieves in a single day (Kuwajima et al., 2013). This difference in clearing time can affect the duration and outcome of the experiment because longer clearing times can increase transparency but also fluorescence quenching. In any case, shorter clearing times are obviously preferable.

Although there is no perfect clearing agent, they are all generally expected to increase transparency, image resolution, and depth of laser and antibody penetration. Although in most cases it is also desirable that they minimally affect tissue integrity and organ size, changes in organ size might be beneficial in some cases. For instance, organ swelling can potentially allow a better analysis of the whole tissue and may also improve image resolution in applications such as expansion microscopy (Murakami et al., 2018). On the other hand, tissue shrinkage can fit the sample into the working distance of the optical system and therefore allow whole organ visualization. Even if some clearing agents quench fluorophores, they are expected to preserve the fluorescence signal when used properly. That is, as the tissue becomes more transparent, light scattering is reduced, and the detection of the fluorescence signal is improved, thus enabling visualization of fluorescence from deeper regions of the tissue provided.

3D IMAGING TECHNIQUES: CONFOCAL, MULTIPHOTON, STIMULATED RAMAN SCATTERING AND LIGHT SHEET FLUORESCENCE MICROSCOPY

Once an organ has been cleared, several techniques enable the acquisition of 3D images. The use of confocal microscopy is limited to the analysis of thin sections, which may suffice for some experimental approaches but not for the generation of whole-organ 3D images. This is because confocal microscopes use objectives of higher magnification, such as 20x or 40x, requiring a shorter working distance, whereas typically in light sheet fluorescence microscopy (LSFM), microscopes use low magnification objectives in the 2x–10x range, capable of imaging larger samples. In addition, the confocal microscope scans the sample sequentially point by point, and thus exposes the sample continuously to laser light, which causes photobleaching, whereas the LSFM microscope generates a light sheet that illuminates a single slice of the sample at a time, thus reducing photobleaching. Multiphoton microscopy also illuminates a single plane at a time, as photon convergence for fluorescent stimulation only occurs at the focal plane (Figure 1A). Although it provides a larger penetration depth than confocal microscopy and is less affected by sample scattering (Costa et al., 2019), it is still unable to image large sample volumes at once. The LSFM setup, with the sample inside a chamber and a long distance from the objective to the sample, makes it possible to analyze larger tissue fragments.

However, similarly to confocal microscopy, LSFM requires fluorescent labeling, hence increasing clearing protocol times. Although LSFM reduces sample exposure to the laser, photobleaching of fluorophores

cannot be fully avoided. To overcome this issue, label-free imaging techniques such as stimulated Raman scattering (SRS) microscopy have been recently developed for 3D imaging with subcellular resolution (Wei et al., 2019) (Figure 1B). SRS microscopy uses the resonant frequency of molecular bonds to detect different cellular components. By irradiating a certain bond type with a pulse laser *Ip* and its corresponding Stoke's frequency *Is* if the frequency difference (Raman shift) matches the quantum height of the vibrational state of the bond, a fraction of *Ip* becomes absorbed and reemitted by stimulated emission as *Is*. The intensity loss of *Ip* is named SRL (stimulated Raman loss), and by detection of its magnitude for different Raman shifts at each point of the sample, image reconstruction can be obtained (Freudiger et al., 2008). However, although recent SRS-specific clearing techniques have been developed to improve the imaging depth of stimulated Raman microscopy, SRS imaging potential regarding sample volume and depth still remains similar to that of confocal (less than 1 mm3 and around 1 mm depth) (Wei et al., 2019). Therefore, LSFM is still the best option for rapid, whole-organ 3D imaging.

In a typical custom-made multispectral light sheet microscope or LSFM, the sample is positioned by means of three motorized stages that allow translation (X, Y, and Z) and a rotation motor (Zaber Technologies, Canada). The imaging system consists of a scientific CMOS camera (Neo, Andor, Northern Ireland) with 2560 × 2160 active pixels and a physical detector size of 6.5 μm × 6.5 μm and a tube lens placed after the emission filter wheel.

The laser unit comprises five different excitation laser lines with powers ranging from 50 to 200 mW (405, 473, 532, 589, and 635 nm). The emission filters available, with widths in the 20-nm range, are 475, 531, 607, 624, and 670 nm. The excitation laser beam is directed through a set of mirrors toward a cylindrical lens (f = 50 mm), which together creates a light sheet of approximately t2 μm thickness.

In LSFM microscopy, the sample is illuminated with a thin light sheet, meaning that only one plane of the sample is illuminated at each time point, in such a way that only the fluorescence emitted from that individual plane is detected (Santi, 2011; Power and Huisken, 2017; Huisken et al., 2004). The plane of the specimen exposed to the light can be selected by moving the sample until all required planes have been illuminated and detected. Therefore, a high-resolution 3D image can be constructed by scanning the whole sample, plane by plane. The working principle of light sheet illumination is illustrated (Figure 1A).

LSFM offers benefits over world-wide used confocal microscopy, which, although is one of the most popular and accessible 3D imaging techniques, for the time being, has important limitations. Under the confocal microscope, the fluorescence signal from non-focal planes is filtered out, but the whole sample remains illuminated during acquisition, producing photobleaching at a rapid rate. The limitations of photobleaching and out-of-focus fluorescence are avoided with LSFM, in which only one plane of the specimen is selectively illuminated at each time point, whereas the rest of the sample is kept in the dark. Hence, fluorophores are not illuminated for long periods, and there is no need to filter out-of-focus fluorescence since only the focal plane produces a signal (Huisken and Stainier, 2009).

TRANSLATIONAL APPLICATIONS OF TISSUE CLEARING AND 3D IMAGING

Recent reports describe the use of different tissue clearing methods for several biological tissues and organs. As discussed above, the method of choice would depend on the transparency of the organ, type of fluorescence, the importance of tissue shrinkage, and clearing time. Here, we summarize tissue-clearing strategies. Note that most of the information available for the tissues was obtained from mouse models and that data for human tissues are still scarce. Different CUBIC cleared mouse organs are shown in Figure 3.

Heart

A recent study compared tissue clearing reagents and protocols based on aqueous solvents to clear embryonic and fetal hearts (Kolesová et al., 2016). CLARITY, SCALE, CUBIC, and dibenzylether (DBE) were compared in terms of transparency and organ size. The authors concluded that the CUBIC method was the best suited to clear the embryonic heart. Furthermore, CUBIC preserved endogenous protein fluorescence well, as confirmed by the detection of the heart GFP signal in a transgenic mouse model (Kolesová et al., 2016). The CUBIC method can also be used to improve confocal imaging of relatively thick mouse heart sections, as it enhances antibody penetration and light detection (Nehrhoff et al., 2016). The whole mouse heart can be cleared with CUBIC allowing 3D vasculature image (Nehrhoff et al., 2017) (Figure 4). A

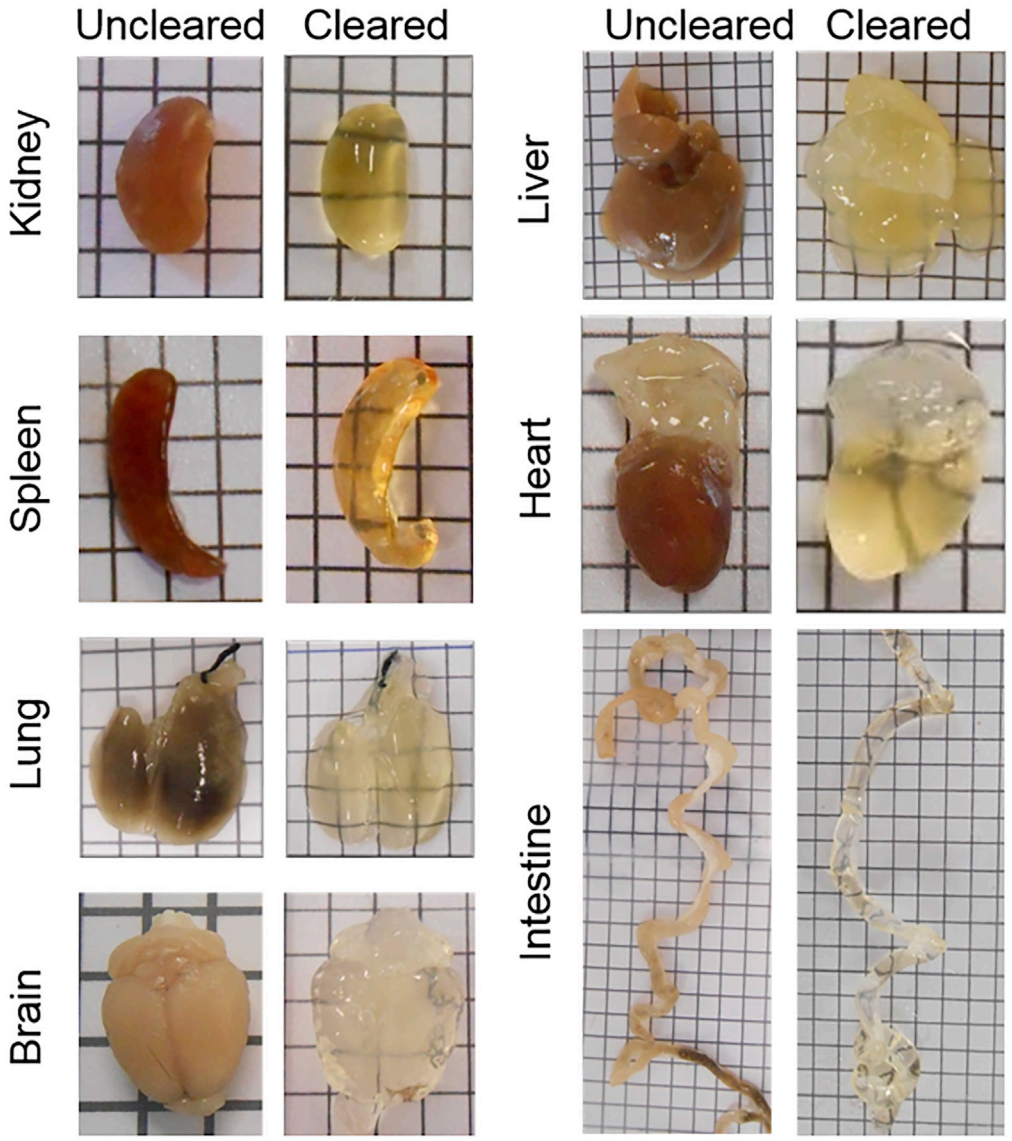

Figure 3. Mouse Tissues Cleared with the CUBIC Protocol

Mice were perfused with 4% PFA and organs were extracted. The CUBIC clearing protocol was adapted to each tissue by changing the clearing time. Cleared and uncleared kidney, spleen, lung, brain, liver, heart, and intestine are shown.

combination of CUBIC and CLARITY, named SUT (Scheme Update on tissue Transparency), has been used to evaluate spatial distribution and phenotype of fibroblasts in mice left ventricles in a post-myocardial infarction (Wang et al., 2018). Additionally, a modified CLARITY method that skips the electrophoretic step named SCM (Simplified CLARITY method) has been applied to mouse heart to study proteins distribution (Sung et al., 2016).

Skeletal Muscle

Skeletal muscle has been cleared with a mixture of reagents *N*, *N*, *N*′, *N*′-Tetrakis(2-hydroxypropyl), ethylenediamine, urea, and RIMS, which are compatible with LacZ staining and fluorescent reporters (Verma et al., 2016). Both confocal microscopy and two-photon microscopy have been used to image the cremaster, diaphragm, digitorum longus, and soleus muscles (Verma et al., 2016). Skeletal muscle is a complex tissue that hosts a variety of cell types, including myocyte syncytia, satellite cells, fibroblasts, and

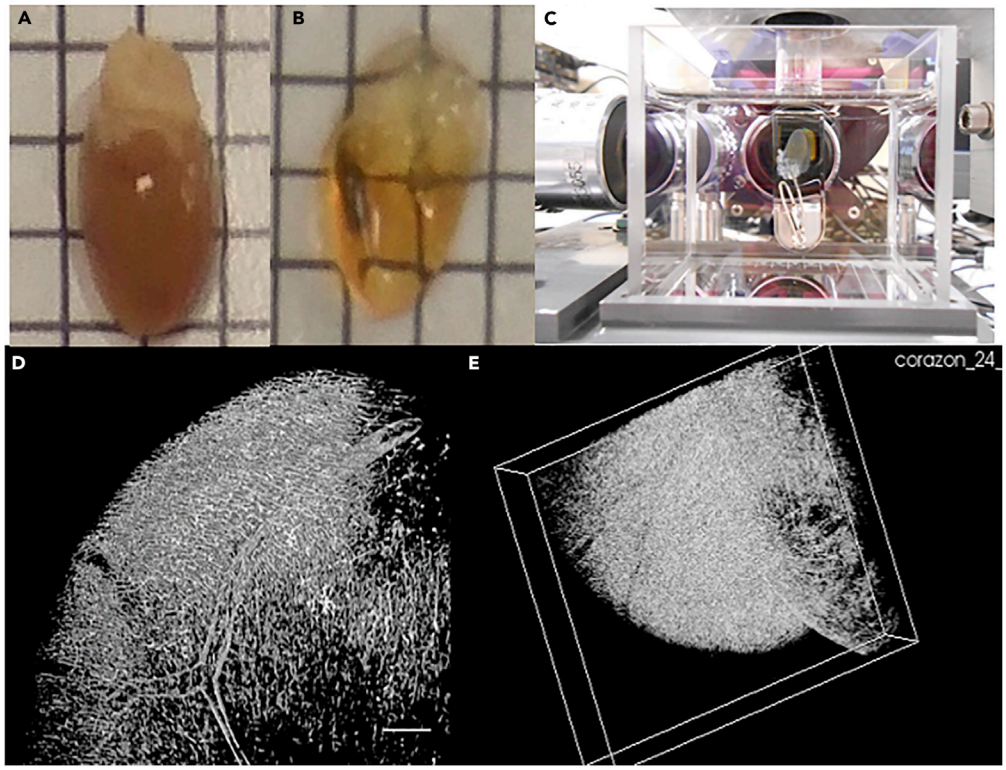

Figure 4. Mouse Hearts Cleared with CUBIC and Vasculature 3D Image

(A and B) Mice were perfused with PFA 4%, and the hearts were removed. The CUBIC clearing protocol was applied in (B); (A) heart without clearing. Length of background squares: 3.85 mm.

(C) CUBIC cleared heart inside the cuvette.

(D and E) SPIM images of mouse heart vasculature. Mice were perfused with PFA 4% and Lectin-649Alexa, and the hearts were removed and cleared with CUBIC protocol. 3D imaging of the heart was acquired with SPIM microscopy using 635 nm excitation laser, and 670 nm emission filter. Stripes artifact was removed with VSNR Fiji plugin, and 3D image rendering was performed with ImageJ. Both images represent different perspectives of the same rendering. Scale bar: 100 microns.

endothelial cells. The combination of clearing reagents and advanced imaging makes it possible to study the connection between various cell populations during development, regeneration, fibrosis, atrophy, and other physiological and pathological processes. Tissue clearing also enables the observation of changes in myofiber organization and vasculature distribution in response to various insults. A report comparing agents used to clear skeletal muscle found that 3DISCO had better clearing properties while preserving the endogenous GFP signal (in transgenic animals) and immunofluorescence from labeled secondary antibodies. In contrast, Clear^{T}, ScaleA2, and CLARITY showed limitations with GFP and/or immunostaining (Decroix et al., 2015). CUBIC has been used for muscle clearing in a mouse model of Duchenne muscular dystrophy (Bozycki et al., 2018). Very recently, a new hydrogel-based tissue clearing method, MYOCLEAR, has been described for the labeling and detection of all neuromuscular junctions and diaphragm muscles in mice to overcome the incompatibility of CLARITY with α-bungarotoxin, which is one of the main Ach-receptor markers (Williams et al., 2019). Lastly, a very recent comparative study of different tissue clearing methods 3DISCO, FDISCO, FRUIT, SeeDB, Sca*l*eS, and CUBIC has been reported for the study of neuromuscular junctions in skeletal muscle (Yin et al., 2019). Clinically, the knowledge of the distributions of the specific structures in the muscles might be used by surgeons to avoid or reduce injuries to peripheral nerves (Yin et al., 2019).

Brain and Neural Tissue

This type of tissue is the most widely studied using tissue clearing methods (Kim et al., 2018; Wan et al., 2018). In principle, it is essential for any method that aims at clearing neural tissue to perform a prior delipidation

step to remove the myelin sheets that enclose neuronal axons (Susaki et al., 2020), as their high lipidic content causes a large amount of scattering. An approach combining CLARITY with double photon microscopy enabled visualization of gray matter in the intact brain (Chang et al., 2017). CLARITY has also been adapted for visualization of astroglia in mice (Miller and Rothstein, 2016). CUBIC was proposed as a new brain clearing method that obviates electrophoresis, in contrast to CLARITY (Susaki et al., 2014). CUBIC's clearing capability of neural tissue has been quantitatively proved by means of a small-angle X-ray scattering analysis (SAXS), which showed that CUBIC reagent 1 is capable of effectively removing the myelin sheet and, therefore, reducing scattering (Susaki et al., 2020). Chicken embryo brains have been successfully cleared with an optimized CUBIC method (Gómez-Gaviro et al., 2017). Mouse brains have been rendered transparent with an alternative CUBIC protocol named CUBIC 1, which uses CUBIC-L and CUBIC-P for the delipidation and discoloration step. The discoloration is achieved by the competitive binding of 1-methylimidazole to heme groups thanks to its structural similarity to histidine in globin. CUBIC 1 also uses CUBIC-R or a cheaper version named CUBIC-RA for RI matching (Tainaka et al., 2018). When using neutral pH solutions, CUBIC1 was able to better preserve tissue volume and microstructure (Tainaka et al., 2018). These CUBIC methods mainly aim at improving the sample's transparency. However, a novel CUBIC pipeline that focuses on immunostaining efficiency has been recently developed, named CUBIC-HistoVIsion. The authors demonstrated the electrolyte-hydrogel behavior of fixed, delipidated tissues, what supports the application of the Lorentz-Lorenz equation (which was stated in 1880 for polymers) to tissues, as mentioned in the introduction (Ueda et al., 2020). They used this resemblance to optimize electrostatic interactions between the dye or immunolabel and the gel, and improve their penetration by regulating pH, salt concentration, temperature, and other environmental and chemical conditions (Susaki et al., 2020).

High-resolution whole-mouse brain atlas has been developed by using an alternatively modified CUBIC protocol, named CUBIC-X. This method uses non-hydrogel-mediated expansion microscopy, by means of imidazole/antipyrine aqueous cocktails, which largely preserve tissue fluorescence and structure (Murakami et al., 2018). PACT has also been adapted for expansion microscopy (ePACT) for Brainbow visualization by an increase in the concentration of SDS used in the protocol (Treweek et al., 2015). Magnified analysis of proteome (MAP) is an alternative expansion microscopy clearing protocol that has been used for super-resolution mouse brain imaging (Mano and Albanese, 2018).

In order to improve the clearing efficiency of neonatal brains, ReagentF was developed as a modification of ClearT by the addition of Triethanolamine (Poola et al., 2019). Alternatively, fetal brain tissue can be cleared by applying 3DISCO in whole embryos (Table 1). This method is quite versatile and can also be used for the study of other organs (Mano and Albanese, 2018). It is particularly advantageous for large ones since the volume shrinkage produced by 3DISCO can make them fit into the small working distances of high-magnification objectives. Ultimate DISCO (uDISCO) was recently reported to clear the whole mouse body (Pan et al., 2016), including calcified bones with no need for a previous decalcification treatment. uDISCO increases the half-life of endogenous fluorescent proteins, reduces clearing time compared with 3DISCO, and uses tert-butanol, which is more stable than 3DISCO's THF. However, it is a more complex protocol, not compatible with tdTomato and increases background fluorescence. A modification of the 3DISCO method, FDISCO (DISCO with superior Fluorescence preservation), has been developed very recently to visualize neurons in the whole brain, to overcome the difficulty of uDISCO to clear myelin-rich tissues (Qi et al., 2019). FDISCO showed better fluorescence conservation, required shorter clearing times, and was compatible with tdTomato. GFP fluorescence preservation has been described modifying the protocol uDisco by addition of alkaline triethylamine for high-quality visualization of neuronal structures and has been called uDISCO (alkaline pH-based uDISCO). This protocol adjusts the pH value of uDISCO to the optimal value for GFP stability to increase endogenous fluorescence and reduce background noise (Li et al., 2018). An alternative modification of 3DISCO, sDISCO (stabilized DISCO), also provides a great GFP fluorescence preservation in mouse brain by adjusting pH to an alkaline value and by using antifading propyl gallate, which prevents fluorophore quenching by reducing decomposition of DBE and BABB into peroxides and aldehydes. Additionally, iDISCO (immunolabeling enabled 3DISCO) has been used in mouse brain to study degeneration of neurons in sensory ganglia. In order to reduce iDISCO-induced tissue shrinking, iDISCO + has been developed by substituting THF by a combination of methanol and dichloromethane with no loss of clearing efficiency (Renier et al., 2016).

ACT-PRESTO (active CLARITY technique-pressure-related efficient and stable transfer of macromolecules into organs) was also used for brain and whole-body clearing with shorter protocols. It seems to be scalable

for larger animals (Lee et al., 2016), thanks to the use of a highly porous hydrogel that allows better removal of lipids and more rapid diffusion of macromolecules, compared with CLARITY. In order to better preserve tissue architecture and fluorescence, an alternative hydrogel-based method named stabilization under harsh conditions via intramolecular epoxide linkages to prevent degradation (SHIELD) has been used to evaluate the synaptic architecture of virally labeled murine neurons at single–cell resolution (Park et al., 2018). Additionally, in order to decrease CLARITY's clearing times and protein loss and increase the signal to noise ratio, Fast free of acrylamide clearing tissue (FACT) was developed by adjusting pH, temperature, and SDS concentration (Xu et al., 2017).

Sca*l*eSQ method has been optimized for brain thick sections. The modified protocol was named IsoSca*l*eSQ and uses NaCl to reduce sample swelling and avoid tissue structure distortion (Sato et al., 2019), similarly to CUBIC1A (Susaki and Ueda, 2016). BABB has been adapted for adult mouse brain by addition of 1-propanol and maintenance of an alkaline media and has been renamed as FluoClearBABB (Schwarz et al., 2015). PACT has been used to clear the whole rat brain by perfusion into the CSF circuitry (PARS-CSF) (Yang et al., 2014a). SeeDB has been modified by combining fructose and urea to obtain an RI matching solution of low viscosity appropriate for large organ clearing by intravital perfusion (Hou et al., 2015). This protocol, named FRUIT, was capable of clearing a whole rabbit brain while retaining the advantages of SeeDB (Hou et al., 2015). SeeDB2 has been introduced to achieve super resolution imaging of mouse brain (Ke et al., 2016) by reducing spherical aberrations caused by RI mismatch. Additionally, in order to provide rapid clearing with FP preservation while maintaining membrane integrity, a novel clearing method named UbasM (Urea-Based Amino Sugar Mixture) has been developed to visualize mouse brains (Chen et al., 2018) and brains diseased from Alzheimer's disease (Chen et al., 2017; Liu et al., 2018), by reducing the amount of delipidation by minimizing the detergent concentration. MXDA-based Aqueous Clearing System (MACS) is a clearing method that has been very recently developed, and that also reduces delipidation, allowing, therefore, lipid staining with DiI labeling or other markers, and that, nevertheless, maintains a high clearing performance. It uses m-xylylenediamine (MXDA), which is a water-miscible liquid with a high refractive Index that induces hyperhydration in a similar way to urea (Zhu et al., 2020).

Combinations of more than one clearing protocol with clearing reagents have also been tested in neural tissues. For example, Passive CLARITY has been combined with TDE to adjust the refraction index and thus clear the mouse central nervous system (Roberts et al., 2016). The reason for choosing TDE is its low cost and adjustable RI, which can reach very high values despite its low viscosity. This may be due to its polarizable sulfur atom (see Table 2). Additionally, iDISCO+ has been combined with Adipo-Clear (see section Adipose Tissue) to improve the clearing of the whole rat brain by further optimization of the delipidation step (Branch et al., 2019).

Skin and Lymph Nodes

Skin can be cleared using agents such as sucrose, fructose, PEG-400 (Zaytsev et al., 2020), PEG-300, salicylic acid (Zhao et al., 2016), glycerol (Zhong et al., 2010), or glucose solutions. These agents are commonly known as SOCAs (skin optical clearing agents) and generally adjust skin refractive indexes and induce packaging of scatterers such as collagen fibers (Tuchina et al., 2019) by dehydration-driven reduction of skin thickness (Wen et al., 2010). Several penetration enhancers are widely used to facilitate their diffusion and improve their clearing power; they can be classified into chemical penetration enhancers such as propylene glycol, DMSO (Zaytsev et al., 2020), ethanol (Zaytsev et al., 2020), azone (Zhao et al., 2016), dimethyl sulfoxide (Genina et al., 2020), oleic acid (Zaytsev et al., 2020), and thiazone (Zaytsev et al., 2020) (the last four ones achieve penetration enhancement by dissolving *Stratum Corneum* lipids) (Zaytsev et al., 2020), and physical penetration enhancers, such as ultrasounds (sonophoresis) (Genina et al., 2020), microneedles (Yoon et al., 2010), lasers (FLMA, fractional laser microablation) (Genina et al., 2020a), pneumatic pressure (Damestani et al., 2014), heat (Damestani et al., 2014), or abrasive instruments (microdermabrasion) (Genina et al., 2020). Different combinations of penetration enhancers have been applied to improve the efficacy of several clearing agents. For instance, PEG-400 has been applied in combination with oleic acid and sonophoresis, improving optical clearing (Zaytsev et al., 2020). Besides, it has been shown that combined application of microneedles and sonophoresis can enhance diffusion rate of 70% glycerol up to 2.3-fold compared with microneedling alone (Yoon et al., 2010) and that FLMA in combination with sonophoresis highly increases clearing speed of PEG-300 (Genina et al., 2020a). Additionally, combination of skin cleaning, microdermabrasion, sonophoresis, and glycerol application allowed improved signal detection in photoacoustic flow cytometry (Menyaev et al., 2013), and merging of propylene glycol, heated to 45°C,

microneedling, vacuum pre-treatment, and application of positive pressure increased porcine skin transparency up to 25% (Damestani et al., 2014).

Skin clearing was found to be useful for the study of the vascular bed, blood flow dynamics, and the response of vessels to vasoactive agents (Guo et al., 2016; Bashkatov et al., 2018). This ability to image live blood flow has fostered the development of *in vivo* flow cytometry in vessels of the mouse ear (Markovic et al., 2013) and has allowed improved detection of circulating tumoral cells in subdermal blood vessels (Menyaev et al., 2013).

A mouse whole body, including the skin, has been successfully cleared and imaged using vDISCO owing to the nanobody-fluorescence boosting of the tissues (Cai et al., 2019). This recently developed technique uses the uDISCO protocol for the clearing step and then performs fluorescence enhancement of GFP by diffusion of nanobodies that carry bright synthetic fluorophores. Nanobodies must have a low molecular weight and recognize fluorescent protein's epitopes, so the variable domain of heavy chain antibodies is used.

Lymph nodes have been cleared with 75% glycerol and Focus clear (Song et al., 2015), both of which make it possible to visualize complex cellular structures and vascular and lymphatic networks and to identify metastasizing melanoma cells deep inside the lymph node cortex. Clearing agents can also be combined with LSFM to study the interaction between T cells and dendritic cells in the lymph node in 3D (Abe et al., 2016; Ozga and Moalli, 2016). Murine lymph nodes have been reported to be cleared with Ce3D too, which has been further applied to many other tissues, providing excellent results regarding tissue transparency, fluorescence and structure preservation, clearing time, and immunostaining (Li et al., 2019) (see Table 1).

Mammary Gland

Although uncleared mammary gland tissue can provide information about structures near the surface, tissue clearing offers a considerable advantage in the study of mammary gland development. Several tissue clearing techniques have been proposed to clear the mouse mammary gland. Lloyd-Lewis et al. compared PACT-RC, PACT-RIMS, 3DISCO, CUBIC, and SeeDB and concluded that See-DB and CUBIC rendered better results in terms of transparency. These methods have been used for the identification of the contribution of different cell clones in the development of this tissue. They also allow healthy and tumor tissue in the gland to be compared and mammary cells to be phenotyped within the tissue (Lloyd-Lewis et al., 2016). Additionally, ScaleSQ has been used to clear breast cancer spheroids and enhance FUCCI fluorescence in deeper regions (Costa et al., 2019).

Kidney

Kidney biopsies have been cleared using the BABB tissue clearing reagent, which enables visualization of changes in glomerular capsule cells that had not been observed in thin tissue sections (Olson et al., 2016). This particular study showed how clearing methods could improve histological analysis by providing superior accuracy. The 3D approach enabled visualization of normal and damaged glomerular capsules and revealed changes in the distribution and morphology of parietal epithelial cells. Recently, comparative studies have been carried out using several reagents and protocols, including Scale and ECI, CLARITY, CUBIC1, and uDISCO, to study crescentic diseases that may include podocyte depletion (Puelles et al., 2019; Masselink et al., 2019). Related to pathologies in the kidney, potassium-mediated tubule remodeling has also been revealed by optical clearing (Saritas et al., 2018) and ethanol-ECi (ethyl-cinnamate) cleared kidneys have enabled the study of renal nephrosis. ECi is a harmless food additive that renders RI matching and pH adjustment for fluorescent protein stability (Klingberg et al., 2017).

Liver

The liver has been cleared with Clear^{T2}, SeeDB, and CUBIC to determine the fate of the DNA vectors used for gene therapy (Fumoto et al., 2016). The ability of CUBIC to reveal the 3D distribution of the transgene was clearly superior, enabling light penetration of 1.5 mm. Nanoparticles in cells or in tissue are better visualized with passive clearing tissue protocols than with electrophoretic methods. Hepatobiliary clearance of nanoparticles was possible with CUBIC but not with electrophoresis (Sindhwani et al., 2017).

Lung

3D imaging of the lungs is particularly useful, as the reconstruction of the whole anatomy of the organ is challenging from small individual images. However, lung tissue has been cleared in very few studies. Benzyl alcohol and benzyl benzoate have been used to clear lung tissue and to study lung innervation (Scott et al., 2014). Lung infection in mice has been studied with CLARITY and PACT, which made it possible to detect *Mycobacterium tuberculosis* granulomas expressing the tomato fluorescent protein as deep as 1 mm into the tissue (Cronan et al., 2015). Fibrillary collagen in whole lung fibrosis can be visualized with BABB (Ochoa et al., 2018). The entire accessory lobe of a fibrotic rat lung has been cleared with CRISTAL (Curing Resin-Infiltrated Sample for Transparent Analysis with Light) and imaged with scanning laser optical tomography with sub-alveolar resolution. CRISTAL encapsulates the specimen in a transparent resin that suppresses sample movement and allows correlative imaging (Kellner et al., 2016).

Intestine, Ovary, and Eye

Murine colon has been cleared for 3D imaging using vertically scanned LSFM (Dong et al., 2014). Image clearing and LSFM microscopy have been applied to both human and mouse intestine samples (Brede et al., 2012). The identification of structural alterations in a murine inflammatory bowel disease model was possible on 3D-reconstructed images of the colon (Arranz et al., 2013). A TDE-based clearing protocol, the iILUmination of Cleared organs to IDentify target molecules method (LUCID), has allowed 3D imaging of gastrointestinal porcine mucosa and may be applicable to human tissues (Mizutani et al., 2018). Ovarian tissue and murine ovarian follicles have been cleared with CUBIC in EGFP transgenic mice (Kagami et al., 2018). In the study of the eye, an intact mouse eye has been cleared with a new protocol called EyeCi, bleaching the melanin with hydrogen peroxide and using solvent-based clearing, which enables ocular and retinal vascular and neovascularization (Henning et al., 2019). CUBIC has also been combined with hydrogen peroxide to clear the mouse eye. Cochlea and organo de corti have been cleared using CUBIC, disco, and CLARITY (Urata et al., 2019).

Hard Tissues

Hard tissues like bones and teeth have been cleared and imaged with a new method called PEGASOS (polyethylene glycol [PEG]-associated solvent system), which uses PEG to protect endogenous fluorescence (Jing et al., 2018). Femur, knee joint, teeth, and mandible have been reconstructed in a 3D manner when these tissues were cleared with this method. PEGASOS has also been shown to clear the intact mouse brain imaging individual neurons and dorsal root ganglions directly through vertebrae. vDISCO and CLARITY have been reported to clear hard tissues as well (Jing et al., 2018). Bones have also been cleared with Ce3D without prior decalcification (Li et al., 2017). CUBIC2 is a modified CUBIC1 protocol that includes CUBIC-B for the decalcification step and has been reported to efficiently clear mouse limbs (Tainaka et al., 2018). PACT-deCAL has been used to clear hard tissues by performing a previous decalcification step in EDTA (Ariel, 2017). Similarly, iDISCO+ has been used to clear rat temporal bone by previously using EDTA and 5% gelatin (Perin et al., 2019). Bone CLARITY has been applied to mice tibia, femur, and vertebral column to view Sox9-tdTomato^{+} fluorescent osteoprogenitor cells (Greenbaum et al., 2017). However, and contrary to PEGASOS, it is not able to clear soft tissues (Jing et al., 2018). Additionally, SeeDB2 has been successfully applied to mouse nasal bone (Ke et al., 2016).

Tumor Tissue

In the field of cancer research, tissue clearing has been used to study tumor development and morphology. Several tissue clearing protocols have been used to visualize tumor vasculature and tumor models (Feuchtinger et al., 2016).

Clearing of melanoma in *in vivo* animal models makes it possible to visualize tumor microvasculature. This is a particularly challenging tissue since pigmentation limits light penetrance. The use of clearing agents on superficial layers of the skin improved melanoma imaging *in vivo* using optical coherent tomography, together with white-light diffuse reflectance spectroscopy, which may have applications for the diagnosis of melanoma (Pires et al., 2016). This particular application is feasible because the skin is an external organ and allows *in vivo* clearing and imaging.

Lung carcinoma has been cleared with the CUBIC protocol combined with intravenous lectin injection, post-labeling antibody-based techniques, and fluorescence in situ hybridization (FISH). These techniques

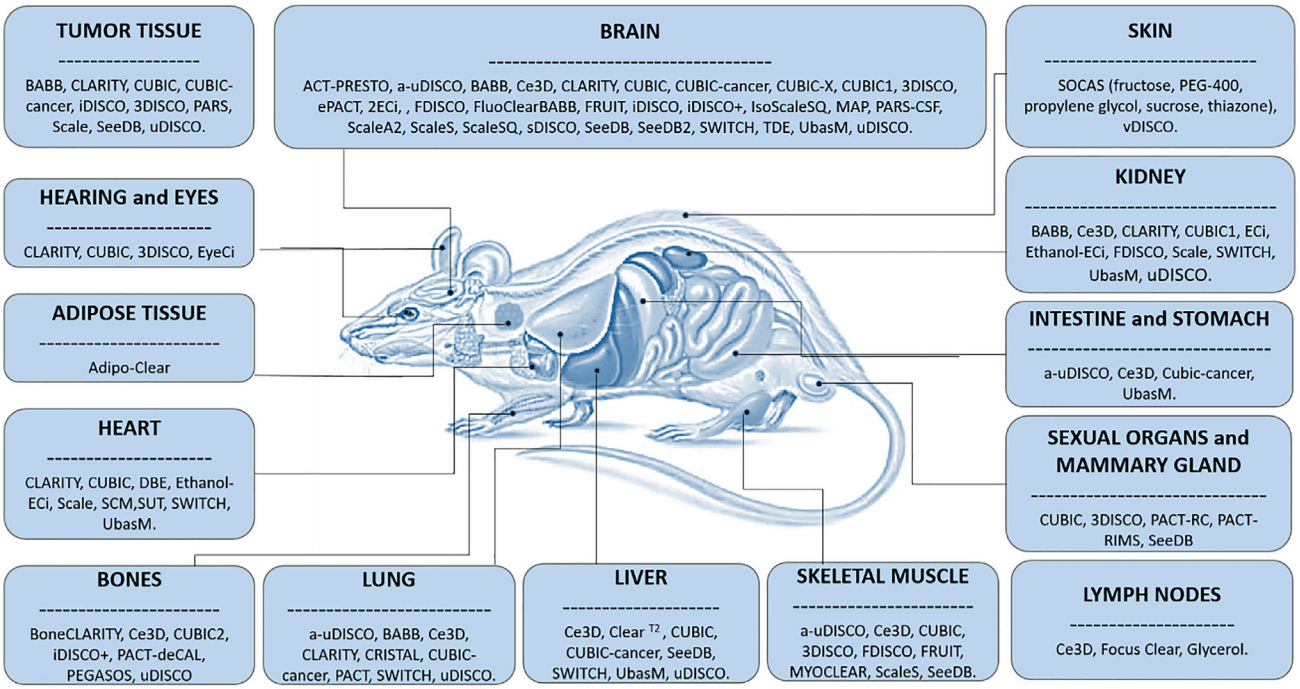

Figure 5. Graphical Summary of Optical Clearing Methods that Have Been Applied So Far to Murine Organs

The mouse image was adapted from Science Photo Library (https://www.sciencephoto.com/media/385863/view/mouse-anatomy#:~:text=This%20image%20is%20not%20available%20for%20purchase%20in%20your%20country).

were used to assess tumor volume and spatial distribution of macrophage infiltration at the cellular level in the whole lung (Cuccarese et al., 2017). An alternative CUBIC protocol named CUBIC-cancer has been applied to evaluate metastasis evolution by analyzing different-stage mouse tumors. Similarly to CUBIC 1 it uses CUBIC-L as the delipidating solution and CUBIC-R for the RI matching step (Kubota et al., 2017).

Prostate specimens and prostate cancer samples have been analyzed with tissue clearing techniques combined with confocal microscopy. Clearing the tissue with BABB increases the depth of penetration to 800 μm, as compared with the 70 μm achieved in uncleared tissue (van Royen et al., 2016).

Pancreatic intraepithelial neoplasms have been analyzed with clearing methods in a duct lesion model. By using "commercial clearing solutions," such as different types of CUBIC reagents provided by TCL America, or Focus Clear and DeepClear provided by CelExplorer, it was possible to unveil distinct growth patterns and the relationship of the tumor cells with the surrounding vessels and microenvironment (Lin et al., 2016). Tissue clearing has also been used for the study of pancreatic islet innervation by neural cells in non-tumoral tissue, revealing neurovascular remodeling (Lin et al., 2016).

Scale, 3Disco, iDisco, uDISCO, SeeDB, and CLARITY have been used for the 3D visualization of gliomas, brain vasculature, and tumor microenvironment, enabling the identification of glioblastoma networks (Lagerweij et al., 2017). UbasM has been applied to murine lung to detect metastases of breast cancer (Chen et al., 2017).

Adipose Tissue

Optically clearing adipose tissue presents a great challenge owing to the large concentration of lipids that it contains, which are mainly responsible for light scattering. To overcome this issue, a modified iDISCO+ protocol named Adipo-Clear was recently published to remove lipids from mouse adipose tissue without altering its structure to study beige fat biogenesis (Chi et al., 2018).

A summary of different protocols and reagents for clearing rodent tissues is represented in Figure 5.

Human Tissues and Diagnostics

Very few studies have analyzed human tissue using clearing protocols, which have mainly focused on biopsy specimens and accessible tissues such as skin (Wang et al., 2012). This growing field has now expanded to *in vivo* tissue clearing approaches in dermatology. The use of topical SOCAs (Table 1) on human skin opens a "window" that enables visualization of the dermal vasculature and deeper tissues (Shi et al., 2017). This approach seems promising for the diagnosis of skin tumors and peripheral vascular diseases (Pires et al., 2016).

The human eye has been cleared using SeeDB, enabling the visualization of choroid and retina (Hohberger et al., 2017). This opens up the possibility for pathologists to study intraocular diseases, such as retinal tumors, which would now be possible in non-dissected eyes.

Tissue clearing has allowed the study of large and small vessels in different human tissues. The aorta has been cleared with BABB in humans and allows discriminating between a healthy abdominal aorta and an aortic aneurysm (Niestrawska et al., 2016). The authors identified severe structural deficiencies in aortic aneurysms, particularly those affecting the collagen fibers surrounding the aorta. Human placental tissue and its vasculature have been imaged in 3D following tissue clearing with CLARITY and X-CLARITY, the latter being able to clear the tissue in half the time (Carrillo et al., 2018). Human gingiva has been cleared with BABB, and iDISCO and light-sheet microscopy have enabled the acquisition of 3D images of capillaries in stromal papillae invading stratified epithelium. Human gingival morphology and vascular structures using patient waste material can be analyzed using this technology (Azaripour et al., 2018).

Human myocardial tissue has been cleared with Free-of-Acrylamide SDS-based Tissue Clearing (FASTClear), which combines iDISCO with a non-hydrogel version of CLARITY (Perbellini et al., 2017). The acquisition of quality images of this tissue is challenging because of its high cellular density. The clearing method used in this work enabled the acquisition of a 3D image of the fibrotic area of an infarcted region and its associated vascular network. This tool allows the accurate analysis of fibrotic tissue distribution within the heart, improving the sensitivity and objectivity of diagnosis and treatments. The human heart has also been cleared with CUBIC3, which is a recently optimized CUBIC protocol designed to obtain a rapid and aggressive clearing. It uses CUBIC-HL for delipidation and also discoloration, and CUBIC-R for the RI matching step. It preserves endogenous proteins better but can hinder fluorescence in some cases (Tainaka et al., 2018).

Tissue clearing protocols have also been applied to the human trachea, unveiling tracheal innervation at all depths. Using this approach, human tracheal tissue compartments can be easily identified and intrinsic airway ganglia can be quantified (Scott et al., 2014). The human pancreas has also been cleared to visualize the neuroinsular network (Butterworth et al., 2018).

Finally, the human brain has been cleared with CLARITY, enabling the direct comparison between MRI-based and microscopy-based 3D histology on aged postmortem brain samples (Morawski et al., 2018). An alternative to CLARITY has been developed to withstand elution and to allow multiplexing imaging of human brain samples by several labeling and delabeling antibody steps. This protocol, named SWITCH (System-Wide control of Interaction Time and kinetics of Chemicals), uses acidic (SWITCH-off) and alkaline (SWITCH-on) solutions to induce homogeneous gel formation in the sample and increase antibody penetration. The resulting GA-BSA gel renders high mechanical, chemical, and thermal stability of the sample, allowing high temperature (and therefore fast) clearing with SDS and reducing agents (Murray et al., 2015). Additionally, both fresh and archival human brains have been cleared with OPTIClear (Optical Properties-adjusting Tissue-Clearing agent), which is an RI matching solution that uses TDE for the hydrophilic brain compartments and iohexol for the hydrophobic ones (Lai et al., 2018). It renders great transparency without a prior delipidation step. It also preserves tissue integrity, although fluorescence is slightly hindered. It has been used with confocal microscopy, but its utility for LSFM has not been studied yet (Lai et al., 2018). The CUBIC protocol has also been modified to clear human brain. By using CUBIC-L as the delipidating and decolorating reagent, and CUBIC-R for the RI matching step, the so-called CUBIC4 is a rapid, FP-compatible and endogenous protein preserving protocol that has a higher clearing performance than conventional CUBIC. A DISCO-based clearing method that focuses on fluorescent labeling has been developed to analyze human cortex cytoarchitecture. This method, named Multiscale Architectonic Staining of Human

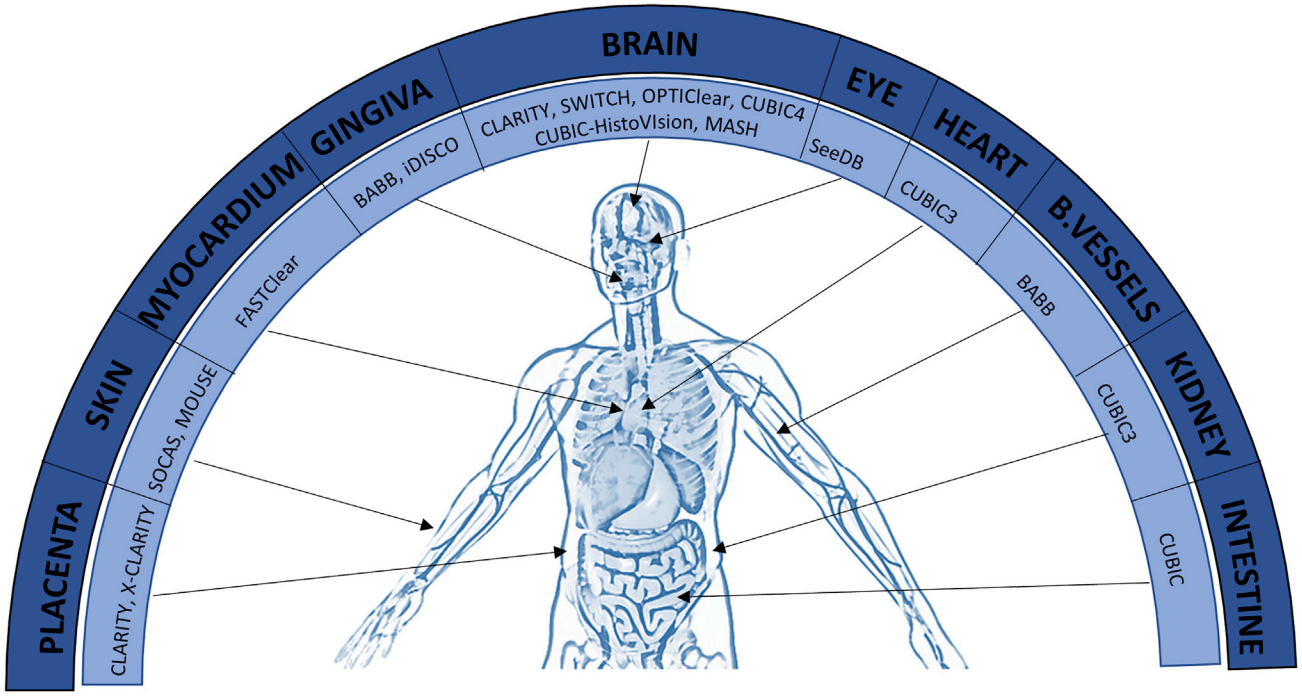

Figure 6. Graphical Summary of All the Optical Clearing Methods that Have Been Applied So Far to Each of the Human Organs or Tissues Mentioned in the Text

The human image was adapted from Shutterstock (https://www.shutterstock.com/es/video/clip-2318627-human-body-internal-organs-loop-rotation).

Cortex (MASH), makes use of small organic fluorescent dyes and a set of adjustable refractive index solutions specially adapted for large human samples (Hildebrand et al., 2018).

Human cerebral organoids have been cleared with 2ECi (second-generation ethyl cinnamate-based clearing method), which was developed to overcome long clearing times of aqueous-based clearing methods and fluorescence quenching of organic solvents (Masselink et al., 2019).

A summary of tissue clearing methods and reagents for human tissues is represented in Figure 6.

OPTICAL CLEARING AND 2D AND 3D IMAGING AS A PATHOLOGY DIAGNOSIS TOOL

Despite the difficulties to clear human tissue, LSM has proved to be an efficient and reliable histopathological tool for biopsy analysis. By performing optical clearing and by means of different types of light sheet microscopy such as OT-LSM, biopsies obtained from kidney, breast, and prostate have been successfully analyzed with a similar subcellular resolution to that obtained by standard histological imaging such as H&E staining. As sample sectioning is not required, optical clearing and 3D imaging can be used to obtain more reliable structural and functional information from the biopsy and, therefore, a more accurate diagnosis. This may be very useful for efficient tumor margin assessment (Poola et al., 2019). Optical clearing has also been presented as a novel 3D histopathology technique for pancreatic lesions diagnosis (Hong et al., 2019).

Optical clearing has shown to increase the efficiency of medical diagnosis by additional imaging systems, such as optical coherence tomography, which allowed subepidermal melanoma identification *in vivo* (Genina et al., 2015), and photoacoustics, which was used for non-invasive detection of glucose content of blood vessels and tissues *in vivo* (Genina et al., 2015). It has also allowed optimization of tissue elasticity analysis by High-Resolution micro-Brillouin spectroscopy (HRmBS) (Rioboo et al., 2019). This novel type of spectrometer-based imaging technique is used to detect intrinsic sound waves of the tissue, which are caused by molecular thermodynamic movement or phonons. The amplitude and frequency of the waves, and therefore their energy, depend on the elasticity of the tissue. When the sample is irradiated with a laser beam, some photons collide with an expanding sound wave that reduces their energy and therefore, their

frequency; others encounter a retreating wave that increases their energy, and the rest of the photons remain unaltered, so for isotropic materials, an output of three main symmetric frequency peaks is obtained, known as the anti-Stokes, Rayleigh, and Stokes peaks. The shift between the peaks is directly dependent on the elasticity constant of the tissue (Rioboo et al., 2019).

The laser beam is reflected by backscattering and directed into the Brillouin spectrometer. The basis of the Fabry-Perot spectrometer is a pair of highly reflective mirrors between which the entering laser suffers constructive or destructive interference with itself. The distance between the mirrors determines the frequency that can escape to the detector. By regulating this distance by means of a piezoelectric device, an almost analog spectroscopic analysis of the laser beam can be performed. Optical clearing of the tissue has been proved to increase the SNR (sound to noise ratio) of the measured signal without modifying the frequency shift, i.e., without altering its physical properties, therefore increasing signal quality and reducing acquisition time (Rioboo et al., 2019).

This technique has promising perspectives for the diagnosis of cardiovascular diseases (Rioboo et al., 2019) or for *in vivo* assessment of skin pathologies since an elasticity change is often a sign of disease. Brillouin microscopy may also be used in clinical practice to detect keratoconus (Yun and Chernyak, 2018). Although there are other currently available techniques such as the atomic force microscopy (AFM) that also provide information regarding the mechanical behavior of the sample, HRmBS is non-invasive and does not require mechanical devices to interact with the sample (Rioboo et al., 2019). However, AFM allows for the computation of Young's elastic modulus, whereas HRmBS can only measure the longitudinal elasticity modulus, which assumes no strain in other directions different from the probing one (Elsayad et al., 2016).

In the coming years, the application of optical clearing as an aid of tissue elasticity analysis or optical imaging for *in vivo* diagnosis of skin pathologies may become a reality. For instance, as mentioned in section Skin and Lymph Nodes, optical clearing has already been applied *in vivo* to mouse ear (Guo et al., 2016) and to rat skin (Mao et al., 2009). A 30% glycerol solution was used as a refractive index matcher of dermic collagen without causing necrosis (Mao et al., 2009). Rat skin has also been cleared *in vivo* with 40% glucose solutions (Tuchina et al., 2019) and with PEG-300 in combination with FLMA/sonophoresis, the latter achieving maximal transparency in 90 min (Genina et al., 2020a).

Optical clearing has been applied *in vivo* to human skin too. Optical clearing with polypropylene glycol-based polymers and polyethylene glycol-based pre-polymer mixture enhanced visibility of telangiectasias to up to 500 μm (Khan et al., 2004). Glycerol has been applied to *in vivo* human skin with prior *Stratum Corneum* removal (Fox et al., 2009), and 40% glucose solutions have been injected subcutaneously inducing long term increased transparency of *in vivo* human dermis (Tuchin et al., 2001). Recently, a novel skin optical clearing method named MOUSE (Microdermabrasion, Oleic acid, and UltraSound Effect) has been successfully applied to human skin *in vivo* (Genina et al., 2020), further increasing light penetration depth to 800 μm. Additionally, and as mentioned in section Tumor Tissue, optical clearing agents have been applied *in vivo* to human melanoma to image microvascular networks (Pires et al., 2016). However, *in vivo* optical clearing is currently focused on the skin only, more specifically dermis, owing to its extension and optical accessibility (Costantini et al., 2019). As an exception, the mouse skull has been optically cleared *in vivo* to image brain microvasculature and neurons at a cortical level by means of two photon microscopy (Zhao et al., 2018).

Still, *in vivo* optical clearing is very limited by the mandatory requirement of chemical and physical biocompatibility with living tissues. Most of the currently available optical clearing methods are chemically aggressive, toxic, or irreversible, narrowing the available range to a few aqueous solutions (Costantini et al., 2019).

DISCUSSION AND FUTURE PERSPECTIVES

Originally described for brain tissue, clearing protocols have been extended to many other tissues. The choice of clearing agent and protocol depends on the specimen, the developmental stage, the characteristics of the tissue to be analyzed, and whether it will be applied *in vivo* or *ex vivo*. The nature and opacity of the tissue and the size of the sample could limit the success of clearing.

Tissue clearing makes possible to overcome some major limitations of (confocal) microscopy for the 3D study of organ structure; however, the approach still faces technical challenges that need to be addressed in the future. To date, tissue clearing has been applied mainly to small animals, with few data reported on human tissue. Human samples are difficult to perfuse, thus potentially generating technical limitations. Furthermore, the large size of human samples is a challenge in the 3D analysis of human tissue.

The development of more novel clearing protocols might minimize the problems of molecular dyes conjugated to antibodies fluorescence quenching, interruption of tissue integrity, endogenous protein fluorescence preservation, and deeper tissue light penetration, which remain challenging. More advanced imaging devices, such as new-generation LSFM with higher image resolution, faster acquisition, and multiple angle illumination, together with more sophisticated post-imaging analysis software, will enable more accurate 3D analysis at cellular (and even subcellular) resolution.

The field of whole-organ imaging at subcellular resolution is moving forward at great speed, mainly due to the advance of new and more efficient clearing protocols, combined with microscopy modalities in biomedical research, clinical diagnosis, and patient follow-up.

CONCLUSIONS

Clearing protocols enable researchers to obtain more accurate optical 3D images of different human and animal tissues. Microanatomy and tissue cytoarchitecture can be analyzed, preserving the tissue structure and providing more accurate data with this emerging technology. The combination of animal models of human diseases with clearing protocols and LSFM imaging enables 3D visualization of organ damage and provide a more accurate basis for diagnosis and treatment.

ACKNOWLEDGMENTS

This work was supported by Ministerio de Ciencia, Innovación y Universidades, ISCIII-FIS grants PI18/00462 co-financed by ERDF, European Union (FEDER) Funds from the European Commission, European Union, "A way of making Europe"; the CNIC is supported by the Ministerio de Ciencia, Innovación y Universidades y the Pro CNIC Foundation, Severo Ochoa Center of Excellence (SEV-2015-0505), CIBER de Salud Mental (CIBERSAM), and COST-action CA16124. J.R. acknowledges funding from EU H2020 FET Open project SENSITIVE, ID 801347, and Ministerio de Ciencia, Innovación y Universidades Grant FIS2016-77892-R. All applicable international, national, and/or institutional guidelines for the care and use of animals were followed. All procedures performed in studies involving animals were in accordance with the ethical standards of the institution or practice at which the studies were conducted.

AUTHOR CONTRIBUTIONS

M.V.G.-G., M.D., and J.R. wrote the paper and obtained the funding. D.S. performed the experiments. M.V.G. coordinated the work.

REFERENCES

Abe, J., Ozga, A.J., Swoger, J., Sharpe, J., Ripoll, J., and Stein, J.V. (2016). Light sheet fluorescence microscopy for in situ cell interaction analysis in mouse lymph nodes. J. Immunol. Methods *431*, 1–10.

Antonacci, G., and Braakman, S. (2016). Biomechanics of subcellular structures by non-invasive Brillouin microscopy. Sci. Rep. *6*, 37217.

Anzai, Y., Minoshima, S., and Lee, V.S. (2019). Enhancing value of MRI: a call for action. J. Magn. Reson. Imaging *49*, e40–e48.

Ariel, P. (2017). A beginner's guide to tissue clearing. Int. J. Biochem. Cell Biol. *84*, 35–39.

Arranz, A., Dong, D., Zhu, S., Rudin, M., Tsatsanis, C., Tian, J., and Ripoll, J. (2013). Helical optical projection tomography. Opt. Express *21*, 25912–25925.

Azaripour, A., Lagerweij, T., Scharfbillig, C., Jadczak, A.E., Willershausen, B., and van Noorden, C.J. (2016). A survey of clearing techniques for 3D imaging of tissues with special reference to connective tissue. Prog. Histochem. Cytochem. *51*, 9–23.

Azaripour, A., Lagerweij, T., Scharfbillig, C., Jadczak, A.E., Swaan, B.V.D., Molenaar, M., Waal, R.V.D., Kielbassa, K., Tigchelaar, W., Picavet, D.I., et al. (2018). Three-dimensional histochemistry and imaging of human gingiva. Sci. Rep. *8*, 1647.

Bashkatov, A.N., Berezin, K.V., Dvoretskiy, K.N., Chernavina, M.L., Genina, E.A., Genin, V.D., Kochubey, V.I., Lazareva, E.N., Pravdin, A.B., Shvachkina, M.E., et al. (2018). Measurement of tissue optical properties in the context of tissue optical clearing. J. Biomed. Opt. *23*, 1–31.

Becker, K., Jährling, N., Saghafi, S., Weiler, R., and Dodt, H.-U. (2012). Chemical clearing and dehydration of GFP expressing mouse brains. PLoS One *7*, e33916.

Bozycki, L., Łukasiewicz, K., Matryba, P., and Pikula, S. (2018). Whole-body clearing, staining and screening of calcium deposits in the mdx mouse model of Duchenne muscular dystrophy. Skeletal Muscle *8*, 21.

Branch, A., Tward, D., Vogelstein, J.T., Wu, Z., and Gallagher, M. (2019). An optimized protocol for iDISCO+ rat brain clearing, imaging, and analysis. bioRxiv, 639674.

Brede, C., Friedrich, M., Jordán-Garrote, A.-L., Riedel, S.S., Bäuerlein, C.A., Heinze, K.G., Bopp, T., Schulz, S., Mottok, A., Kiesel, C., et al. (2012). Mapping immune processes in intact tissues at cellular resolution. J. Clin. Invest. *122*, 4439–4446.

Butterworth, E., Dickerson, W., Vijay, V., Weitzel, K., Cooper, J., Atkinson, E.W., Coleman, J.E., Otto, K.J., and Campbell-Thompson, M. (2018). High resolution 3D imaging of the human pancreas neuro-insular network. J. Vis. Exp. *131*, 56859.

Cai, R., Pan, C., Ghasemigharagoz, A., Todorov, M.I., Förstera, B., Zhao, S., Bhatia, H.S., Parra-Damas, A., Mrowka, L., Theodorou, D., et al. (2019). Panoptic imaging of transparent mice reveals whole-body neuronal projections and skull-meninges connections. Nat. Neurosci. *22*, 317–327.

Carrillo, M., Chuecos, M., Gandhi, K., Bednov, A., Moore, D.L., Maher, J., Ventolini, G., Ji, G., and Schlabritz-Loutsevitch, N. (2018). Optical tissue clearing in combination with perfusion and immunofluorescence for placental vascular imaging. Medicine (Baltimore) *97*, e12392.

Chang, E.H., Argyelan, M., Aggarwal, M., Chandon, T.S., Karlsgodt, K.H., Mori, S., and Malhotra, A.K. (2017). The role of myelination in measures of white matter integrity: combination of diffusion tensor imaging and two-photon microscopy of CLARITY intact brains. Neuroimage *147*, 253–261.

Chen, L., Li, G., Li, Y., Li, Y., Zhu, H., Tang, L., French, P., Mcginty, J., and Ruan, S. (2017). UbasM: an effective balanced optical clearing method for intact biomedical imaging. Sci. Rep. *7*, 12218.

Chen, L., Li, G., Li, Y., Liu, L., Liu, A., and Ruan, S. (2018). UbasM: A Simple, Rapid, Efficient Balanced Optical Clearing Method for Brain Imaging (SPIE).

Chi, J., Wu, Z., Choi, C.H.J., Nguyen, L., Tegegne, S., Ackerman, S.E., Crane, A., Marchildon, F., Tessier-Lavigne, M., and Cohen, P. (2018). Three-dimensional adipose tissue imaging reveals regional variation in beige fat biogenesis and PRDM16-dependent sympathetic neurite density. Cell Metab. *27*, 226–236.e3.

Chung, K., Wallace, J., Kim, S.-Y., Kalyanasundaram, S., Andalman, A.S., Davidson, T.J., Mirzabekov, J.J., Zalocusky, K.A., Mattis, J., Denisin, A.K., et al. (2013). Structural and molecular interrogation of intact biological systems. Nature *497*, 332–337.

Costa, E.C., Silva, D.N., Moreira, A.F., and Correia, I.J. (2019). Optical clearing methods: an overview of the techniques used for the imaging of 3D spheroids. Biotechnol. Bioeng. *116*, 2742–2763.

Costantini, I., Ghobril, J.P., di Giovanna, A.P., Allegra Mascaro, A.L., Silvestri, L., Mullenbroich, M.C., Onofri, L., Conti, V., Vanzi, F., Sacconi, L., et al. (2015). A versatile clearing agent for multi-modal brain imaging. Sci. Rep. *5*, 9808.

Costantini, I., Cicchi, R., Silvestri, L., Vanzi, F., and Pavone, F.S. (2019). In-vivo and ex-vivo optical clearing methods for biological tissues: review. Biomed. Opt. Express *10*, 5251–5267.

Cronan, M.R., Rosenberg, A.F., Oehlers, S.H., Saelens, J.W., Sisk, D.M., Jurcic Smith, K.L., Lee, S., and Tobin, D.M. (2015). CLARITY and PACT-based imaging of adult zebrafish and mouse for whole-animal analysis of infections. Dis. Models Mech. *8*, 1643–1650.

Cuccarese, M.F., Dubach, J.M., Pfirschke, C., Engblom, C., Garris, C., Miller, M.A., Pittet, M.J., and Weissleder, R. (2017). Heterogeneity of macrophage infiltration and therapeutic response in lung carcinoma revealed by 3D organ imaging. Nat. Commun. *8*, 14293.

Damestani, Y., Melakeberhan, B., Rao, M.P., and Aguilar, G. (2014). Optical clearing agent perfusion enhancement via combination of microneedle poration, heating and pneumatic pressure. Lasers Surg. Med. *46*, 488–498.

Decroix, L., van Muylder, V., Desender, L., Sampaolesi, M., and Thorrez, L. (2015). Tissue clearing for confocal imaging of native and bio-artificial skeletal muscle. Biotech. Histochem. *90*, 424–431.

Dodt, H.-U., Leischner, U., Schierloh, A., Jahrling, N., Mauch, C.P., Deininger, K., Deussing, J.M., Eder, M., Zieglgansberger, W., and Becker, K. (2007). Ultramicroscopy: three-dimensional visualization of neuronal networks in the whole mouse brain. Nat. Methods *4*, 331–336.

Dong, D., Arranz, A., Zhu, S., Yang, Y., Shi, L., Wang, J., Shen, C., Tian, J., and Ripoll, J. (2014). Vertically scanned laser sheet microscopy. J. Biomed. Opt. *19*, 106001.

Elsayad, K., Werner, S., Gallemí, M., Kong, J., Sánchez Guajardo, E.R., Zhang, L., Jaillais, Y., Greb, T., and Belkhadir, Y. (2016). Mapping the subcellular mechanical properties of live cells in tissues with fluorescence emission–Brillouin imaging. Sci. Signal. *9*, rs5.

Erturk, A., Lafkas, D., and Chalouni, C. (2014). Imaging cleared intact biological systems at a cellular level by 3DISCO. J. Vis. Exp. *89*, 51382.

Fedorov, A., Beichel, R., Kalpathy-Cramer, J., Finet, J., Fillion-Robin, J.-C., Pujol, S., Bauer, C., Jennings, D., Fennessy, F., Sonka, M., et al. (2012). 3D slicer as an image computing platform for the quantitative imaging network. Magn. Reson. Imaging *30*, 1323–1341.

Feuchtinger, A., Walch, A., and Dobosz, M. (2016). Deep tissue imaging: a review from a preclinical cancer research perspective. Histochem. Cell Biol. *146*, 781–806.

Fox, M.A., Diven, D.G., Sra, K., Boretsky, A., Poonawalla, T., Readinger, A., Motamedi, M., and McNichols, R.J. (2009). Dermal scatter reduction in human skin: a method using controlled application of glycerol. Lasers Surg. Med. *41*, 251–255.

Freudiger, C.W., Min, W., Saar, B.G., Lu, S., Holtom, G.R., He, C., Tsai, J.C., Kang, J.X., and Xie, X.S. (2008). Label-free biomedical imaging with high sensitivity by stimulated Raman scattering microscopy. Science *322*, 1857–1861.

Fumoto, S., Nishimura, K., Nishida, K., and Kawakami, S. (2016). Three-dimensional imaging of the intracellular fate of plasmid DNA and transgene expression: ZsGreen1 and tissue clearing method CUBIC are an optimal combination for multicolor deep imaging in murine tissues. PLoS One *11*, e0148233.

Genina, E.A., Bashkatov, A.N., and Tuchin, V.V. (2010). Tissue optical immersion clearing. Expert Rev. Med. Devices *7*, 825–842.

Genina, E., Bashkatov, A., Sinichkin, Y., Yanina, I., and Tuchin, V. (2015). Optical clearing of biological tissues: prospects of application in medical diagnostics and phototherapy. J. Biomed. Photon. Eng. *1*, 22–58.

Genina, E.A., Bashkatov, A.N., Terentyuk, G.S., and Tuchin, V.V. (2020a). Integrated effects of fractional laser microablation and sonophoresis on skin immersion optical clearing in vivo. J. Biophotonics *13*, e202000101.

Genina, E.A., Surkov, Y.I., Serebryakova, I.A., Bashkatov, A.N., Tuchin, V.V., and Zharov, V.P. (2020b). Rapid ultrasound optical clearing of human light and dark skin. IEEE Trans. Med. Imaging *99*, 1.

Gómez-Gaviro, M.V., Balaban, E., Bocancea, D., Lorrio, M.T., Pompeiano, M., Desco, M., Ripoll, J., and Vaquero, J.J. (2017). Optimized CUBIC protocol for three-dimensional imaging of chicken embryos at single-cell resolution. Development *144*, 2092–2097.

Greenbaum, A., Chan, K.Y., Dobreva, T., Brown, D., Balani, D.H., Boyce, R., Kronenberg, H.M., Mcbride, H.J., and Gradinaru, V. (2017). Bone CLARITY: clearing, imaging, and computational analysis of osteoprogenitors within intact bone marrow. Sci. Transl. Med. *9*, eaah6518.

Guo, L., Shi, R., Zhang, C., Zhu, D., Ding, Z., and Li, P. (2016). Optical coherence tomography angiography offers comprehensive evaluation of skin optical clearing in vivo by quantifying optical properties and blood flow imaging simultaneously. J. Biomed. Opt. *21*, 081202.

Haass-Koffler, C.L., Naeemuddin, M., and Bartlett, S.E. (2012). An analytical tool that quantifies cellular morphology changes from three-dimensional fluorescence images. J. Vis. Exp. *66*, 4233.

Hahn, C., Becker, K., Saghafi, S., Pende, M., Avdibašić, A., Foroughipour, M., Heinz, D.E., Wotjak, C.T., and Dodt, H.-U. (2019). High-resolution imaging of fluorescent whole mouse brains using stabilised organic media (sDISCO). J. Biophotonics *12*, e201800368.

Hama, H., Kurokawa, H., Kawano, H., Ando, R., Shimogori, T., Noda, H., Fukami, K., Sakaue-Sawano, A., and Miyawaki, A. (2011). Scale: a chemical approach for fluorescence imaging and reconstruction of transparent mouse brain. Nat. Neurosci. *14*, 1481–1488.

Hama, H., Hioki, H., Namiki, K., Hoshida, T., Kurokawa, H., Ishidate, F., Kaneko, T., Akagi, T., Saito, T., Saido, T., and Miyawaki, A. (2015). ScaleS: an optical clearing palette for biological imaging. Nat. Neurosci. *18*, 1518–1529.

Henning, Y., Osadnik, C., and Malkemper, E.P. (2019). EyeCi: optical clearing and imaging of immunolabeled mouse eyes using light-sheet fluorescence microscopy. Exp. Eye Res. *180*, 137–145.

Hikspoors, J.P.J.M., Peeters, M.M.J.P., Mekonen, H.K., Kruepunga, N., Mommen, G.M.C., Cornillie, P., Köhler, S.E., and Lamers, W.H. (2017). The fate of the vitelline and umbilical veins during the development of the human liver. J. Anat. *231*, 718–735.

Hildebrand, S., Schueth, A., Herrler, A., Galuske, R., and Roebroeck, A. (2018). Scalable cytoarchitectonic characterization of large intact human neocortex samples. bioRxiv, 274985.

Hirashima, T., and Adachi, T. (2015). Procedures for the quantification of whole-tissue immunofluorescence images obtained at single-cell resolution during murine tubular organ development. PLoS One *10*, e0135343.

Hohberger, B., Baumgart, C., and Bergua, A. (2017). Optical clearing of the eye using the See Deep Brain technique. Eye *31*, 1496.

Hong, S.M., Noe, M., Hruban, C.A., Thompson, E.D., Wood, L.D., and Hruban, R.H. (2019). A "clearer" view of pancreatic pathology: a review of tissue clearing and advanced microscopy techniques. Adv. Anat. Pathol. *26*, 31–39.

Hou, B., Zhang, D., Zhao, S., Wei, M., Yang, Z., Wang, S., Wang, J., Zhang, X., Liu, B., Fan, L., et al. (2015). Scalable and DiI-compatible optical clearance of the mammalian brain. Front. Neuroanat. *9*, 19.

Huisken, J., and Stainier, D.Y. (2009). Selective plane illumination microscopy techniques in developmental biology. Development *136*, 1963–1975.

Huisken, J., Swoger, J., del Bene, F., Wittbrodt, J., and Stelzer, E.H. (2004). Optical sectioning deep inside live embryos by selective plane illumination microscopy. Science *305*, 1007–1009.

Inyushin, M., Meshalkina, D., Zueva, L., and Zayas-Santiago, A. (2019). Tissue transparency in vivo. Molecules *24*, 2388.

Jianru, W., Tingting, Y., Yisong, Q. and Zhu, D. A Simple Optical Clearing Method for Tissue Block. 2015 Opto-Electronics and Communications Conference (OECC), 28 June-2 July 2015 2015. 1-3.

Jing, D., Zhang, S., Luo, W., Gao, X., Men, Y., Ma, C., Liu, X., Yi, Y., Bugde, A., Zhou, B.O., et al. (2018). Tissue clearing of both hard and soft tissue organs with the PEGASOS method. Cell Res. *28*, 803–818.

Kagami, K., Shinmyo, Y., Ono, M., Kawasaki, H., and Fujiwara, H. (2018). Three-dimensional evaluation of murine ovarian follicles using a modified CUBIC tissue clearing method. Reprod. Biol. Endocrinol. *16*, 72.

Ke, M.T., and Imai, T. (2014). Optical clearing of fixed brain samples using SeeDB. Curr. Protoc. Neurosci. *66*. Unit 2.22.

Ke, M.T., Fujimoto, S., and Imai, T. (2013). SeeDB: a simple and morphology-preserving optical clearing agent for neuronal circuit reconstruction. Nat. Neurosci. *16*, 1154–1161.

Ke, M.T., Nakai, Y., Fujimoto, S., Takayama, R., Yoshida, S., Kitajima, T.S., Sato, M., and Imai, T. (2016). Super-resolution mapping of neuronal circuitry with an index-optimized clearing agent. Cell Rep. *14*, 2718–2732.

Kellner, M., Heidrich, M., Lorbeer, R.A., Antonopoulos, G.C., Knudsen, L., Wrede, C., Izykowski, N., Grothausmann, R., Jonigk, D., Ochs, M., et al. (2016). A combined method for correlative 3D imaging of biological samples from macro to nano scale. Sci. Rep. *6*, 35606.

Khan, M.H., Choi, B., Chess, S., Kelly, M.K., McCullough, J., and Nelson, J.S. (2004). Optical clearing of in vivo human skin: implications for light-based diagnostic imaging and therapeutics. Lasers Surg. Med. *34*, 83–85.

Kim, J.H., Jang, M.J., Choi, J., Lee, E., Song, K.-D., Cho, J., Kim, K.-T., Cha, H.-J., and Sun, W. (2018). Optimizing tissue-clearing conditions based on analysis of the critical factors affecting tissue-clearing procedures. Sci. Rep. *8*, 12815.

Klingberg, A., Hasenberg, A., Ludwig-Portugall, I., Medyukhina, A., Mann, L., Brenzel, A., Engel, D.R., Figge, M.T., Kurts, C., and Gunzer, M. (2017). Fully automated evaluation of total glomerular number and capillary tuft size in nephritic kidneys using lightsheet microscopy. J. Am. Soc. Nephrol. *28*, 452–459.

Kolesová, H., Čapek, M., Radochová, B., Janáček, J., and Sedmera, D. (2016). Comparison of different tissue clearing methods and 3D imaging techniques for visualization of GFP-expressing mouse embryos and embryonic hearts. Histochem. Cell Biol. *146*, 141–152.

Kubota, S.I., Takahashi, K., Nishida, J., Morishita, Y., Ehata, S., Tainaka, K., Miyazono, K., and Ueda, H.R. (2017). Whole-body profiling of cancer metastasis with single-cell resolution. Cell Rep. *20*, 236–250.

Kuwajima, T., Sitko, A.A., Bhansali, P., Jurgens, C., Guido, W., and Mason, C. (2013). ClearT: a detergent- and solvent-free clearing method for neuronal and non-neuronal tissue. Development *140*, 1364–1368.

Křížek, P., Lukeš, T., Ovesný, M., Fliegel, K., and Hagen, G.M. (2016). SIMToolbox: a MATLAB toolbox for structured illumination fluorescence microscopy. Bioinformatics *32*, 318–320.

Lagerweij, T., Dusoswa, S.A., Negrean, A., Hendrikx, E.M.L., de Vries, H.E., Kole, J., Garcia-Vallejo, J.J., Mansvelder, H.D., Vandertop, W.P., Noske, D.P., et al. (2017). Optical clearing and fluorescence deep-tissue imaging for 3D quantitative analysis of the brain tumor microenvironment. Angiogenesis *20*, 533–546.

Lai, H.M., Liu, A.K.L., Ng, H.H.M., Goldfinger, M.H., Chau, T.W., Defelice, J., Tilley, B.S., Wong, W.M., Wu, W., and Gentleman, S.M. (2018). Next generation histology methods for three-dimensional imaging of fresh and archival human brain tissues. Nat. Commun. *9*, 1066.

Lee, E., Choi, J., Jo, Y., Kim, J.Y., Jang, Y.J., Lee, H.M., Kim, S.Y., Lee, H.J., Cho, K., Jung, N., et al. (2016). ACT-PRESTO: rapid and consistent tissue clearing and labeling method for 3-dimensional (3D) imaging. Sci. Rep. *6*, 18631.

Leischner, U., Schierloh, A., Zieglgänsberger, W., and Dodt, H.-U. (2010). Formalin-induced fluorescence reveals cell shape and morphology in biological tissue samples. PLoS One *5*, e10391.

Li, W., Germain, R.N., and Gerner, M.Y. (2017). Multiplex, quantitative cellular analysis in large tissue volumes with clearing-enhanced 3D microscopy (Ce3D). Proc. Natl. Acad. Sci. U S A *114*, E7321–E7330.

Li, Y., Xu, J., Wan, P., Yu, T., and Zhu, D. (2018). Optimization of GFP fluorescence preservation by a modified uDISCO clearing protocol. Front. Neuroanat. *12*, 67.

Li, W., Germain, R.N., and Gerner, M.Y. (2019). High-dimensional cell-level analysis of tissues with Ce3D multiplex volume imaging. Nat. Protoc. *14*, 1708–1733.

Lin, P.-Y., Peng, S.-J., Shen, C.-N., Pasricha, P.J., and Tang, S.-C. (2016). PanIN-associated pericyte, glial, and islet remodeling in mice revealed by 3D pancreatic duct lesion histology. Am. J. Physiol. Gastrointest. Liver Physiol. *311*, G412–G422.

Liu, L., Liu, A., Xiao, W., Li, R., Hu, X. and Chen, L. Volumetric fluorescence imaging combined with modified optical clearing for Alzheimer's disease pathology. 2018 Asia Communications and Photonics Conference (ACP), 26-29 Oct. 2018 2018. 1-3.

Lloyd-Lewis, B., Davis, F.M., Harris, O.B., Hitchcock, J.R., Lourenco, F.C., Pasche, M., and Watson, C.J. (2016). Imaging the mammary gland and mammary tumours in 3D: optical tissue clearing and immunofluorescence methods. Breast Cancer Res. *18*, 127.

Mano, T., and Albanese, A. (2018). Whole-brain analysis of cells and circuits by tissue clearing and light-sheet microscopy. J. Neurosci. *38*, 9330–9337.

Mao, Z., Han, Z., Wen, X., Luo, Q., and Zhu, D. (2009). Influence of Glycerol with Different Concentrations on Skin Optical Clearing and Morphological Changes in Vivo (SPIE).

Markovic, S., Li, B., Pera, V., Sznaier, M., Camps, O., and Niedre, M. (2013). A computer vision approach to rare cell in vivo fluorescence flow cytometry. Cytometry A *83*, 1113–1123.

Masselink, W., Reumann, D., Murawala, P., Pasierbek, P., Taniguchi, Y., Bonnay, F., Meixner, K., Knoblich, J.A., and Tanaka, E.M. (2019). Broad applicability of a streamlined ethyl cinnamate-based clearing procedure. Development *146*, dev166884.

Matryba, P., Kaczmarek, L., and Gołąb, J. (2019). Advances in ex situ tissue optical clearing. Laser Photon. Rev. *13*, 1800292.

Menyaev, Y.A., Nedosekin, D.A., Sarimollaoglu, M., Juratli, M.A., Galanzha, E.I., Tuchin, V.V., and Zharov, V.P. (2013). Optical clearing in photoacoustic flow cytometry. Biomed. Opt. Express *4*, 3030–3041.

Miller, S.J., and Rothstein, J.D. (2016). Astroglia in thick tissue with super resolution and cellular reconstruction. PLoS One *11*, e0160391.

Mizutani, H., Ono, S., Ushiku, T., Kudo, Y., Ikemura, M., Kageyama, N., Yamamichi, N., Fujishiro, M., Someya, T., Fukayama, M., et al. (2018). Transparency-enhancing technology allows three-dimensional assessment of

gastrointestinal mucosa: a porcine model. Pathol. Int. *68*, 102–108.

Morawski, M., Kirilina, E., Scherf, N., Jager, C., Reimann, K., Trampel, R., Gavriilidis, F., Geyer, S., Biedermann, B., Arendt, T., and Weiskopf, N. (2018). Developing 3D microscopy with CLARITY on human brain tissue: towards a tool for informing and validating MRI-based histology. Neuroimage *182*, 417–428.

Moy, A.J., Wiersma, M.P., and Choi, B. (2013). Optical histology: a method to visualize microvasculature in thick tissue sections of mouse brain. PLoS One *8*, e53753.

Murakami, T.C., Mano, T., Saikawa, S., Horiguchi, S.A., Shigeta, D., Baba, K., Sekiya, H., Shimizu, Y., Tanaka, K.F., Kiyonari, H., et al. (2018). A three-dimensional single-cell-resolution whole-brain atlas using CUBIC-X expansion microscopy and tissue clearing. Nat. Neurosci. *21*, 625–637.

Murray, E., Cho, J.H., Goodwin, D., Ku, T., Swaney, J., Kim, S.Y., Choi, H., Park, Y.G., Park, J.Y., Hubbert, A., et al. (2015). Simple, scalable proteomic imaging for high-dimensional profiling of intact systems. Cell *163*, 1500–1514.

Nehrhoff, I., Bocancea, D., Vaquero, J., Vaquero, J.J., Ripoll, J., Desco, M., and Gómez-Gaviro, M.V. (2016). 3D imaging in CUBIC-cleared mouse heart tissue: going deeper. Biomed. Opt. Express *29*, 3716–3720.

Nehrhoff, I., Ripoll, J., Samaniego, R., Desco, M., and Gómez-Gaviro, M.V. (2017). Looking inside the heart: a see-through view of the vascular tree. Biomed. Opt. Express *8*, 3110–3118.

Niestrawska, J.A., Viertler, C., Regitnig, P., Cohnert, T.U., Sommer, G., and Holzapfel, G.A. (2016). Microstructure and mechanics of healthy and aneurysmatic abdominal aortas: experimental analysis and modelling. J. R. Soc. Interface *13*, 20160620.

Ochoa, L.F., Kholodnykh, A., Villarreal, P., Tian, B., Pal, R., Freiberg, A.N., Brasier, A.R., Motamedi, M., and Vargas, G. (2018). Imaging of murine whole lung fibrosis by large scale 3D microscopy aided by tissue optical clearing. Sci. Rep. *8*, 13348.

Olson, E., Levene, M.J., and Torres, R. (2016). Multiphoton microscopy with clearing for three dimensional histology of kidney biopsies. Biomed. Opt. Express *7*, 3089–3096.

Ozga, A.J., and Moalli, F. (2016). pMHC affinity controls duration of CD8+ T cell-DC interactions and imprints timing of effector differentiation versus expansion. J. Exp. Med. *213*, 2811–2829.

Pan, C., Cai, R., Quacquarelli, F.P., Ghasemigharagoz, A., Lourbopoulos, A., Matryba, P., and Plesnila, N. (2016). Shrinkage-mediated imaging of entire organs and organisms using uDISCO. Nat. Methods *13*, 859–867.

Park, Y.-G., Sohn, C.H., Chen, R., McCue, M., Yun, D.H., Drummond, G.T., Ku, T., Evans, N.B., Oak, H.C., Trieu, W., et al. (2018). Protection of tissue physicochemical properties using polyfunctional crosslinkers. Nat. Biotechnol. *37*, 73.

Pende, M., Becker, K., Wanis, M., Saghafi, S., Kaur, R., Hahn, C., Pende, N., Foroughipour, M., Hummel, T., and Dodt, H.-U. (2018). High-resolution ultramicroscopy of the developing and adult nervous system in optically cleared *Drosophila melanogaster*. Nat. Commun. *9*, 4731.

Pende, M., Vadiwala, K.P., Schmidbaur, H., Stockinger, A., Murawala, P., Saghafi, S., Dekens, M., Becker, K., Revilla-I-Domingo, R., Papadopoulos, S.-C., et al. (2020). A versatile depigmentation, clearing, and labeling method for exploring nervous system diversity. Sci. Adv. *6*, eaba0365.

Perbellini, F., Liu, A.K.L., Watson, S., Bardi, I., Rothery, S., and Terracciano, C. (2017). Free-of-Acrylamide SDS-based Tissue Clearing (FASTClear) for three dimensional visualization of myocardial tissue. Sci. Rep. *7*, 5188.

Perin, P., Voigt, F.F., Bethge, P., Helmchen, F., and Pizzala, R. (2019). iDISCO+ for the study of neuroimmune architecture of the rat auditory brainstem. Front. Neuroanat. *13*, 15.

Pires, L., Demidov, V., Vitkin, I.A., Bagnato, V., Kurachi, C., and Wilson, B.C. (2016). Optical clearing of melanoma in vivo: characterization by diffuse reflectance spectroscopy and optical coherence tomography. J. Biomed. Opt. *21*, 081210.

Poola, P.K., Afzal, M.I., Yoo, Y., Kim, K.H., and Chung, E. (2019). Light sheet microscopy for histopathology applications. Biomed. Eng. Lett. *9*, 279–291. http://europepmc.org/abstract/MED/31456889.

Power, R.M., and Huisken, J. (2017). A guide to light-sheet fluorescence microscopy for multiscale imaging. Nat. Methods *14*, 360–373.

Puelles, V.G., Fleck, D., Ortz, L., Papadouri, S., Strieder, T., Boehner, A., van der Wolde, J.W., Vogt, M., Saritas, T., Kuppe, C., et al. (2019). Novel 3D analysis using optical tissue clearing documents the evolution of murine rapidly progressive glomerulonephritis. Kidney Int. *96*, 505–516.

Qi, Y., Yu, T., Xu, J., Wan, P., Ma, Y., Zhu, J., Li, Y., Gong, H., Luo, Q., and Zhu, D. (2019). FDISCO: advanced solvent-based clearing method for imaging whole organs. Sci. Adv. *5*, eaau8355.

Renier, N., Wu, Z., Simon, D.J., Yang, J., Ariel, P., and Tessier-Lavigne, M. (2014). iDISCO: a simple, rapid method to immunolabel large tissue samples for volume imaging. Cell *159*, 896–910.

Renier, N., Adams, E.L., Kirst, C., Wu, Z., Azevedo, R., Kohl, J., Autry, A.E., Kadiri, L., Umadevi Venkataraju, K., Zhou, Y., et al. (2016). Mapping of brain activity by automated volume analysis of immediate early genes. Cell *165*, 1789–1802.

Richardson, D.S., and Lichtman, J.W. (2015). Clarifying tissue clearing. Cell *162*, 246–257.

Richardson, D.S., and Lichtman, J.W. (2017). SnapShot: tissue clearing. Cell *171*, 496–496.e1.

Rioboo, R.J.J., Desco, M., and Gomez-Gaviro, M.V. (2019). Impact of optical tissue clearing on the Brillouin signal from biological tissue samples. Biomed. Opt. Express *10*, 2674–2683.

Roberts, D.G., Johnsonbaugh, H.B., Spence, R.D., and MacKenzie-Graham, A. (2016). Optical clearing of the mouse central nervous system using passive CLARITY. J. Vis. Exp. *112*, 54025.

van Royen, M.E., Verhoef, E.I., Kweldam, C.F., van Cappellen, W.A., Kremers, G.J., Houtsmuller, A.B., and van Leenders, G.J. (2016). Three-dimensional microscopic analysis of clinical prostate specimens. Histopathology *69*, 985–992.

Santi, P.A. (2011). Light sheet fluorescence microscopy: a review. J. Histochem. Cytochem. *59*, 129–138.

Saritas, T., Puelles, V.G., Su, X.T., McCormick, J.A., Welling, P.A., and Ellison, D.H. (2018). Optical clearing in the kidney reveals potassium-mediated tubule remodeling. Cell Rep. *25*, 2668–2675.e3.

Sato, Y., Miyawaki, T., Ouchi, A., Noguchi, A., Yamaguchi, S., and Ikegaya, Y. (2019). Quick visualization of neurons in brain tissues using an optical clearing technique. Anat. Sci. Int. *94*, 199–208.

Schindelin, J., Arganda-Carreras, I., Frise, E., Kaynig, V., Longair, M., Pietzsch, T., Preibisch, S., Rueden, C., Saalfeld, S., Schmid, B., et al. (2012). Fiji: an open-source platform for biological-image analysis. Nat. Methods *9*, 676–682.

Schwarz, M.K., Scherbarth, A., Sprengel, R., Engelhardt, J., Theer, P., and Giese, G. (2015). Fluorescent-protein stabilization and high-resolution imaging of cleared, intact mouse brains. PLoS One *10*, e0124650.

Scott, G.D., Blum, E.D., Fryer, A.D., and Jacoby, D.B. (2014). Tissue optical clearing, three-dimensional imaging, and computer morphometry in whole mouse lungs and human airways. Am. J. Respir. Cell Mol. Biol. *51*, 43–55.

Sharpe, J., Ahlgren, U., Perry, P., Hill, B., Ross, A., Hecksher-Sorensen, J., Baldock, R., and Davidson, D. (2002). Optical projection tomography as a tool for 3D microscopy and gene expression studies. Science *296*, 541–545.

Shi, R., Guo, L., Zhang, C., Feng, W., Li, P., Ding, Z., and Zhu, D. (2017). A useful way to develop effective in vivo skin optical clearing agents. J. Biophoton. *10*, 887–895.

Sindhwani, S., Syed, A.M., Wilhelm, S., and Chan, W.C.W. (2017). Exploring passive clearing for 3D optical imaging of nanoparticles in intact tissues. Bioconjug. Chem. *28*, 253–259.

Singh, A., McMullen, J.D., Doris, E.A., and Zipfel, W.R. (2015). Comparison of objective lenses for multiphoton microscopy in turbid samples. Biomed. Opt. Express *6*, 3113–3127.

Song, E., Seo, H., Choe, K., Hwang, Y., Ahn, J., Ahn, S., and Kim, P. (2015). Optical clearing based cellular-level 3D visualization of intact lymph node cortex. Biomed. Opt. Express *6*, 4154–4164.

Sung, K., Ding, Y., Ma, J., Chen, H., Huang, V., Cheng, M., Yang, C.F., Kim, J.T., Eguchi, D., di Carlo, D., et al. (2016). Simplified three-dimensional tissue clearing and incorporation of colorimetric phenotyping. Sci. Rep. *6*, 30736.

Susaki, E.A., and Ueda, H.R. (2016). Whole-body and whole-organ clearing and imaging techniques with single-cell resolution: toward

organism-level systems biology in mammals. Cell Chem. Biol. *23*, 137–157.

Susaki, E.A., Tainaka, K., Perrin, D., Kishino, F., Tawara, T., Watanabe, T.M., Yokoyama, C., Onoe, H., Eguchi, M., Yamaguchi, S., et al. (2014). Whole-brain imaging with single-cell resolution using chemical cocktails and computational analysis. Cell *157*, 726–739.

Susaki, E.A., Shimizu, C., Kuno, A., Tainaka, K., Li, X., Nishi, K., Morishima, K., Ono, H., Ode, K.L., Saeki, Y., et al. (2020). Versatile whole-organ/body staining and imaging based on electrolyte-gel properties of biological tissues. Nat. Commun. *11*, 1982.

Tainaka, K., Murakami, T.C., Susaki, E.A., Shimizu, C., Saito, R., Takahashi, K., Hayashi-Takagi, A., Sekiya, H., Arima, Y., Nojima, S., et al. (2018). Chemical landscape for tissue clearing based on hydrophilic reagents. Cell Rep. *24*, 2196–2210.e9.

Treweek, J.B., Chan, K.Y., Flytzanis, N.C., Yang, B., Deverman, B.E., Greenbaum, A., Lignell, A., Xiao, C., Cai, L., Ladinsky, M.S., et al. (2015). Whole-body tissue stabilization and selective extractions via tissue-hydrogel hybrids for high-resolution intact circuit mapping and phenotyping. Nat. Protoc. *10*, 1860–1896.

Tuchin, V.V., Bashkatov, A.N., Genina, É.A., Sinichkin, Y.P., and Lakodina, N.A. (2001). In vivo investigation of the immersion-liquid-induced human skin clearing dynamics. Tech. Phys. Lett. *27*, 489–490.

Tuchina, D.K., Timoshina, P.A., Tuchin, V.V., Bashkatov, A.N., and Genina, E.A. (2019). Kinetics of rat skin optical clearing at topical application of 40%Glucose: ex vivo and in vivo studies. IEEE J. Sel. Top. Quant. Electron. *25*, 1–8.

Ueda, H.R., Dodt, H.-U., Osten, P., Economo, M.N., Chandrashekar, J., and Keller, P.J. (2020). Whole-brain profiling of cells and circuits in mammals by tissue clearing and light-sheet microscopy. Neuron *106*, 369–387.

Urata, S., Iida, T., Yamamoto, M., Mizushima, Y., Fujimoto, C., Matsumoto, Y., Yamasoba, T., and Okabe, S. (2019). Cellular cartography of the organ of Corti based on optical tissue clearing and machine learning. Elife *8*, e40946.

Verma, M., Murkonda, B.S., Asakura, Y., and Asakura, A. (2016). Skeletal muscle tissue clearing for LacZ and fluorescent reporters, and immunofluorescence staining. Methods Mol. Biol. *1460*, 129–140.

Wan, P., Zhu, J., Xu, J., Li, Y., Yu, T., and Zhu, D. (2018). Evaluation of seven optical clearing methods in mouse brain. Neurophotonics *5*, 035007.

Wang, Z., Shi, X.-Y., Yin, J., Zuo, G., Zhang, J., and Chen, G. (2012). Role of autophagy in early brain injury after experimental subarachnoid hemorrhage. J. Mol. Neurosci. *46*, 192–202.

Wang, Z., Zhang, J., Fan, G., Zhao, H., Wang, X., Zhang, J., Zhang, P., and Wang, W. (2018). Imaging transparent intact cardiac tissue with single-cell resolution. Biomed. Opt. Express *9*, 423–436.

Wei, M., Shi, L., Shen, Y., Zhao, Z., Guzman, A., Kaufman, L.J., Wei, L., and Min, W. (2019). Volumetric chemical imaging by clearing-enhanced stimulated Raman scattering microscopy. Proc. Natl. Acad. Sci. U S A *116*, 6608–6617.

Wen, X., Mao, Z., Han, Z., Tuchin, V.V., and Zhu, D. (2010). In vivo skin optical clearing by glycerol solutions: mechanism. J. Biophotonics *3*, 44–52.

Willadsen, M., Chaise, M., Yarovoy, I., Zhang, A.Q., and Parashurama, N. (2018). Engineering molecular imaging strategies for regenerative medicine. Bioeng. Transl. Med. *3*, 232–255.

Williams, M.P.I., Rigon, M., Straka, T., Hörner, S.J., Thiel, M., Gretz, N., Hafner, M., Reischl, M., and Rudolf, R. (2019). A novel optical tissue clearing protocol for mouse skeletal muscle to visualize endplates in their tissue context. Front. Cell. Neurosci. *13*, 49.

Xu, N., Tamadon, A., Liu, Y., Ma, T., Leak, R.K., Chen, J., Gao, Y., and Feng, Y. (2017). Fast free-of-acrylamide clearing tissue (FACT)—an optimized new protocol for rapid, high-resolution imaging of three-dimensional brain tissue. Sci. Rep. *7*, 9895.

Yang, B., Treweek, J.B., Kulkarni, R.P., Deverman, B.E., Chen, C.-K., Lubeck, E., Shah, S., Cai, L., and Gradinaru, V. (2014a). Single-cell phenotyping within transparent intact tissue through whole-body clearing. Cell *158*, 945–958.

Yang, B., Treweek, J.B., Kulkarni, R.P., Deverman, B.E., Chen, C.K., Lubeck, E., Shah, S., Cai, L., and Gradinaru, V. (2014b). Single-cell phenotyping within transparent intact tissue through whole-body clearing. Cell *158*, 945–958.

Yin, X., Yu, T., Chen, B., Xu, J., Chen, W., Qi, Y., Zhang, P., Li, Y., Kou, Y., Ma, Y., et al. (2019). Spatial distribution of motor endplates and its adaptive change in skeletal muscle. Theranostics *9*, 734–746.

Yoon, J., Park, D., Son, T., Seo, J., Nelson, J.S., and Jung, B. (2010). A physical method to enhance transdermal delivery of a tissue optical clearing agent: combination of microneedling and sonophoresis. Lasers Surg. Med. *42*, 412–417.

Yu, T., Zhu, J., Li, Y., Ma, Y., Wang, J., Cheng, X., Jin, S., Sun, Q., Li, X., Gong, H., et al. (2018). RTF: a rapid and versatile tissue optical clearing method. Sci. Rep. *8*, 1964.

Yun, S.H., and Chernyak, D. (2018). Brillouin microscopy: assessing ocular tissue biomechanics. Curr. Opin. Ophthalmol. *29*, 299–305.

Zaytsev, S., Svenskaya, Y., Lengert, E., Terentyuk, G., Bashkatov, A., Tuchin, V., and Genina, E. (2020). Optimized skin optical clearing for Optical Coherence Tomography monitoring of encapsulated drug delivery through the hair follicles. J. Biophoton. *13*, e201960020.

Zhao, Q., Dai, C., Fan, S., Lv, J., and Nie, L. (2016). Synergistic efficacy of salicylic acid with a penetration enhancer on human skin monitored by OCT and diffuse reflectance spectroscopy. Sci. Rep. *6*, 34954.

Zhao, Y.J., Yu, T.T., Zhang, C., Li, Z., Luo, Q.M., Xu, T.H., and Zhu, D. (2018). Skull optical clearing window for in vivo imaging of the mouse cortex at synaptic resolution. Light Sci. Appl. *7*, 17153.

Zhong, H.-Q., Guo, Z., Wei, H., Zeng, C.-C., Xiong, H., He, Y., and Liu, S. (2010). In vitro study of ultrasound and different-concentration glycerol-induced changes in human skin optical attenuation assessed with optical coherence tomography. J. Biomed. Opt. *15*, 036012.

Zhu, J., Yu, T., Li, Y., Xu, J., Qi, Y., Yao, Y., Ma, Y., Wan, P., Chen, Z., Li, X., et al. (2020). MACS: rapid aqueous clearing system for 3D mapping of intact organs. Adv. Sci. *7*, 1903185.